ABSTRACT

AN EXPERIMENTAL TEST OF THE

ISOBARIC MULTIPLET MASS EQUATION

by George Frederick Trentelman

The ground state mass excesses of ^{9}C, ^{13}O, and ^{21}Mg have been determined through measurement of the Q-values of the $^{12}C(^{3}He,^{6}He)^{9}C$, $^{16}O(^{3}He,^{6}He)^{13}O$, $^{24}Mg(^{3}He,^{6}He)^{21}Mg$ reactions. These mass excesses represent the $T_z = -3/2$ members of the $T = 3/2$ quartets for $A = 9$, 13, and 21 respectively, and for ^{13}O and ^{21}Mg represent measurements of improved accuracy. These experimental values for the quartet members are used to test the isobaric multiplet mass equation (IMME)

$$M(\alpha,T,T_z) = a(\alpha,T) + b(\alpha,T)T_z + c(\alpha,T)T_z^2$$

The measurements were made using 68-70 MeV ^{3}He beams, and a split pole magnetic spectrograph as an energy analyzer. An energy calibration procedure for the spectrograph and beam analysis system with proton and ^{3}He beams has been developed, and has proven valuable in making precision Q-value measurements at high bombarding energies.

The mass excess of ^{9}C has been measured as 28.911±.009 MeV, that of ^{13}O as 23.103±.014 MeV, and that of ^{21}Mg as 10.912±.018 MeV.

In addition, Coulomb radii for a uniformly charged sphere model for A = 9, 13, and 21 have been extracted from the coefficients of the IMME.

AN EXPERIMENTAL TEST OF THE ISOBARIC MULTIPLET MASS EQUATION

by

George Frederick Trentelman

A THESIS

Submitted to

Michigan State University

in partial fulfillment of the requirements

for the degree of

DOCTOR OF PHILOSOPHY

Department of Physics

1970

TABLE OF CONTENTS

LIST OF TABLES

LIST OF FIGURES

1. INTRODUCTION

The purpose of this work is to determine the ground state mass excesses of ^{9}C, ^{13}O, and ^{21}Mg. These ground state masses represent the neutron deficient $T_z = -3/2$ members of the $T = 3/2$ isobaric quartets for A = 9, 13, and 21 respectively, and with the exception of ^{9}C are the least well determined members of these quartets. Since the isobaric multiplet concept appears to be a very sound one, as evidenced by the similar level structure of mirror nuclei and by T = 1 states in even A, T = 1 triplets, it is of interest to extend the study of these multiplets to the T = 3/2 quartets.

The basic contention of the isobaric multiplet concept is that the multiplet members have essentially identical nuclear properties, and differ only through charge dependent effects. The T = 1/2 mirror nuclei are good examples of this. The level schemes for the T = 1/2 mirror pairs ^{17}O and ^{17}F as well as ^{13}C and ^{13}N are shown in figure 1.1. Here the level schemes, with the exception of the first excited states are very similar, and the ground state energy differences between members of each pair may be attributed to the Coulomb energy difference (plus, of course, the proton neutron mass difference). The descrepencies in the first excited states have been attributed to shell effects (No 69), and do not represent a breakdown of Coulomb systematics.

Further verification of the multiplet concept has come from the discovery of isobaric analog states. These states were first observed through the (p,n) reaction by Anderson and Wong (An 62) in a study of

nuclei from A = 48 to A = 93. In each case there was a strong neutron peak whose (p,n) Q-value corresponded exactly to the Coulomb energy difference between the target nucleus and the residual nucleus having the same A, but with one more proton and one less neutron (T differing by 1). The strong yield from these states indicates a similarity between its structure and that of its analog.

Other analog states have been observed as compound nucleus resonances formed, for example, by Target + p $\rightarrow$ excited nucleus $\rightarrow$ Target + p reaction. Here, the center of mass energy of the incident proton must be exactly that required to excite the compound nucleus (Target + p) to one of its analog levels. Normally, these would be the $T_{target} \pm 1/2$ levels. In some cases, however, forbidden analog states ($T_{target} \pm 3/2$) are observed again as resonances, found at high excitation energies and characterized by narrow decay widths. An example of this is the forbidden T = 3/2 level in the system:

$$^{28}Si + p \rightarrow {}^{29}P^{*} \rightarrow {}^{28}Si + p \quad \text{(Te 69 and Ka 70)}.$$

Here the lowest T = 3/2 level is the analog of the ^{29}Si ground state. Finding such strong resonant behavior at high excitation again indicates a similarity between this state and the relatively simple structure of the ^{29}Si ground state.

In the T = 3/2 quartets (and multiplets of higher order) the comparison of the nuclear level schemes becomes more difficult. First, the T = 3/2 levels in the $T_z = \pm 1/2$ members analagous to the $T_z = \pm 3/2$ ground states lie at high excitations ($\sim$15 MeV in the A = 9 multiplet) and in some cases are unbound. This makes energy levels above these states difficult to define. Secondly, the neutron deficient $T_z = -3/2$

(ground state) members lie far from beta stability and are difficult to measure experimentally. Excited states of these members have yet to be determined.

The isospin formalism does, however, provide an expression that connects members of these multiplets in a direct manner. This is the isobaric mass multiplet equation (IMME).

$$M(\alpha,T,T_z) = a(\alpha,T) + b(\alpha,T)\ T_z + c(\alpha,T)\ T_z^2.$$

M is the mass of a nucleus, T its isospin, and T_z its isospin projection. In essence, it is the expansion of a nuclear mass in terms of its isospin characteristics, and is particularly applicable to isobaric multiplets of $T \gg 1$ where the constants a,b, and c may be determined emperically. If the isobaric multiplet assumption that all members are identical in nuclear characteristics and differ only by charge effects is valid, then such an expansion of the multiplet masses in T_z is valid.

This equation may be derived from first order perturbation theory, this is shown in Appendix A1, but fundamentally it comes from two assumptions. (Wi 57)

1. The Coulomb energy is a perturbation on the nuclear energy (valid for light nuclei) and may be expressed as:

$$V_C = \sum_{i>j}^{A} \frac{e^2}{r_{ij}} (1/2 - t_{zi})(1/2 - t_{zj})$$

(as a two body force). The T_z dependence comes from this. In addition, the proton-neutron mass difference may be expressed as:

$$V(\Delta m) = (M_n + M_p)A + (M_n - M_p)\, T_z.$$

2. The specifically nuclear properties of multiplet members are identical and may be characterized by a common set of quantum numbers (designated by α in the equation).

Since the equation is quadratic in T_z, knowledge of isobaric quartets are required to test it. Since this expression engulfs the basic concepts of isobaric multiplets, one of the goals of this experiment is to test it rigorously with well determined T = 3/2 quartets.

The IMME is a rather insensitive probe of particular charge dependent phenomena in itself. The fact that very good IMME fits to the data of isobaric quartets may be obtained, for example, does not necessarily mean that the assumptions from which it may be derived are necessarily true. The reason for this lies in the fact that the quadratic nature of the equation enables it to absorb many other phenomena as perturbations with accuracy sufficient to fit existing data well. This is discussed in detail by Janecke, Garvey, and by Wilkinson (Ja 69), (Ga 69), (Wi 64). In particular, the spin-orbit interaction may be encompassed into isotensors of rank zero, one, and two:

$$V_{so} = \frac{\mu_0 e}{Mc} \sum \left(\left[\frac{g_n + g_p}{4} + \frac{g_n - g_p}{3}\, t_i \cdot t_j \right] + \left[-\frac{g_p}{2}\,(t_{zi} + t_{zj}) + \frac{g_n}{2}\,(t_{zi} - t_{zj}) \right] + \left[(g_n - g_p)\left(t_{zi} t_{zj} - \frac{t_i \cdot t_j}{3} \right) \right] \right) \frac{s_i \cdot l_{ij}}{r_{ij}^3}$$

The derivation of this is found in (Ga 69) where it is pointed out that this effect can be of the order of 50 KeV.

If information on the specifics of charge dependent interactions are to be deduced from the IMME, the isobaric multiplets of $T \geq 3/2$ over as wide a range of A as possible must be measured very accurately. This might then allow trends of A dependence to be determined, and allow deviations between the equation predictions and experimental measurements to become apparent. In fact, the most accurately measured T = 3/2 multiplet, (A = 9), has shown indications of a non-zero term proportional to T_z^3. This indicates that charge dependent perturbation terms above the first order may be needed. (Ce 68) and (Ga 69).

It is of interest then to determine the masses of the T = 3/2 multiplet members as accurately as possible to test the IMME.

The procedure adopted here is to measure the masses of ^{9}C, ^{13}O, and ^{21}Mg by experimentally determining the Q-values of the reactions: $^{12}C(^{3}He,^{6}He)^{9}C$, $^{16}O(^{3}He,^{6}He)^{13}O$ and $^{24}Mg(^{3}He,^{6}He)^{21}Mg$. This required the design of new measurement techniques which are described in what follows.

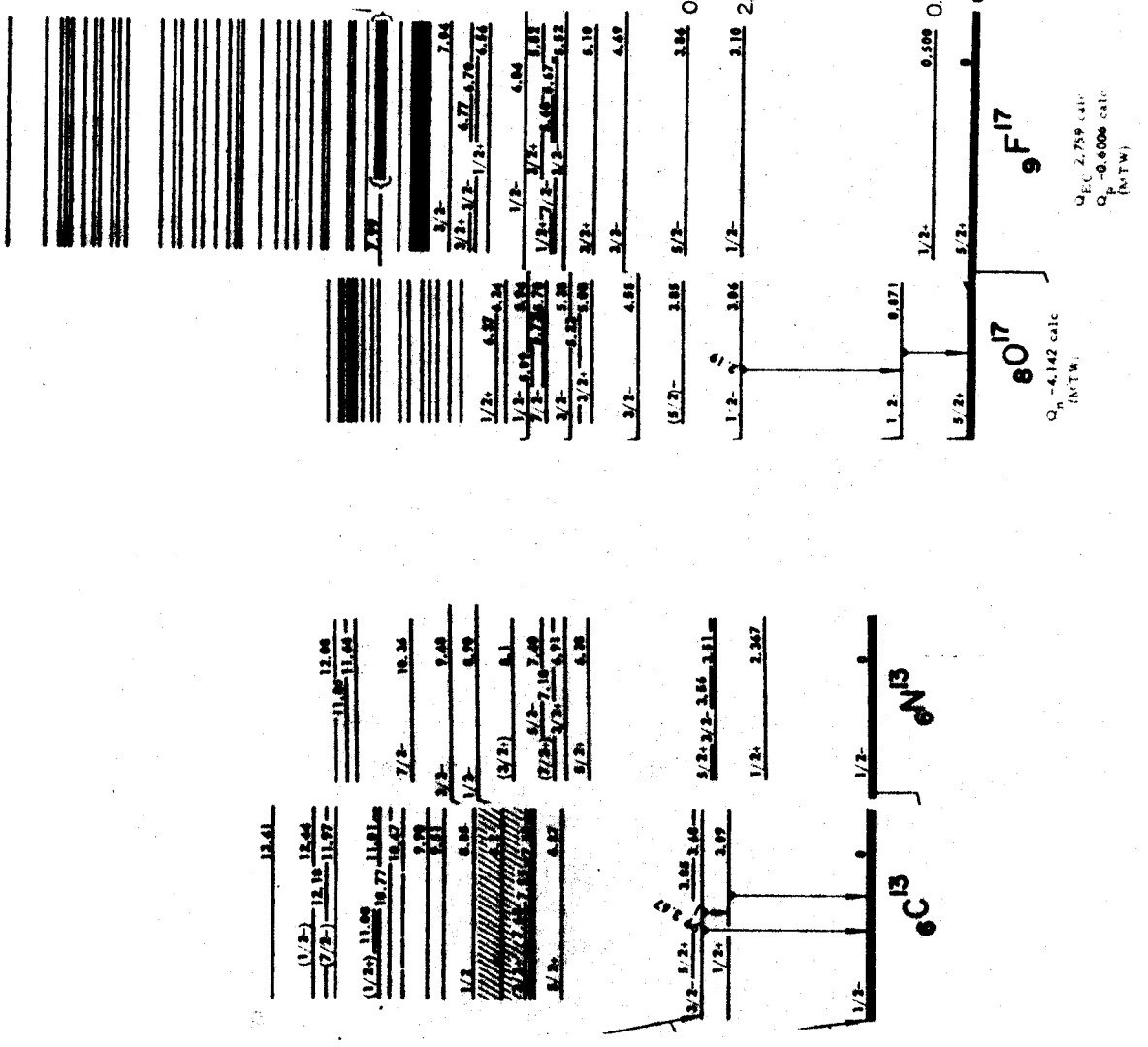

Figure 1.1
Mirror pairs

2. EXPERIMENTAL PROCEDURE

2.1 Introduction

A direct measurement of the (^{3}He,^{6}He) reaction Q-values consists of four major parts:

1. An accurate determination of the incident ^{3}He beam energy
2. An equally accurate determination of the outgoing ^{6}He energy
3. A measurement of the laboratory scattering angle at which the reaction is observed
4. A measurement of the effect of target thickness on incident and outgoing particles.

The determination of these parameters and knowledge of the reaction kinematics is sufficient to determine the Q-value. The mass of the residual nucleus may then be calculated since the masses of ^{3}He, ^{6}He and the target nuclei are known.

Two particular problems arise in measuring (^{3}He,^{6}He) Q-values. First, the cross sections are small (3 μb/sr or less) and this means low yield of ^{6}He for the 150 to 300 nanoamp beam intensities used. Second, the ^{3}He and ^{6}He energy losses in the required target materials are substantial. As an example, E(loss) = 90.2 KeV for 37 MeV ^{6}He in a 432 μg/cm^2 SiO target, and E(loss) = 32.8 KeV for 68 MeV ^{3}He in the same target. The uncertainty involved in measuring these target energy losses becomes a major contributor to the total experimental uncertainty

of the Q-value for target thickness greater than 500 $\mu g/cm^2$. The limits on target thickness and beam intensity restrict the ^6He count rate for a given solid angle. The result is that stringent requirements are placed on the stability of experimental equipment such as electronics, beam transport elements, targets (deterioration), and particularly beam energy. These must remain stable for periods of time sufficient to obtain enough statistics for meaningful analysis.

Two procedures remain available for maximizing the count rate: observing the reaction at a scattering angle where the cross section is a maximum, and using the largest possible solid angle. In this experiment the optimum scattering angle was determined by taking a $^{12}C(^3He,^6He)^9C$ angular distribution between θ_L = 9° to 19°. This angular distribution was taken using a 760 $\mu g/cm^2$ carbon foil, and consequently some energy resolution was sacrificed. This distribution is displayed in figure 2.1. As shown, the distribution peaks at θ_L = 11.0°, and most of the data was taken here.

The solid angle was maximized by using a double focussing split-pole magnetic spectrograph as an energy analyzer. The spectrograph compensates for the kinematic energy spread of the reaction products (132KeV/deg for the $^{12}C(^3He,^6He)^9C$ reaction at θ_L = 10°) by focussing the kinematically spread particles on the focal plane (En 58 and Sp 67). This allowed a solid angle of 1.2 msr to be used.

In addition, magnetic analysis of the reaction products was an aid in obtaining clean ^6He spectra. In particular, the magnetic rigidity of the elastically scattered ^3He was less than that of the ^6He for the beam energies used, and for this reason the elastic ^3He

peak and its low energy tail was prohibited from reaching the focal plane detector while ^{6}He data was being taken. This reduced background in the spectra and made clean particle identification possible.

2.2 Spectrograph Calibration

An accurate energy calibration of the spectrograph is fundamental to this experiment since the spectrograph is used to determine the beam energies, and the energies of the outgoing ^{6}He. Since the only direct information from the spectrograph is the magnitude of the magnetic field in the flat field region between the large pole tips as measured by an NMR probe and the position on the focal plane where the analyzed reaction products are incident, a method of determining particle energies with respect to these two parameters was devised. This calibration technique consists basically of three parts:

1. A calibration involving a reaction with accurately known beam energy and reaction product magnetic rigidities ($B\rho$). This serves to define an effective radius of curvature through the spectrograph, ρ(effective), relative to a focal plane position.

2. A calibration of the field behavior relative to the NMR reading for reaction products passing through the spectrograph along ρ(effective). This calibrates the spectrograph at excitations required for measuring ^{3}He beam and ^{6}He energies.

3. Calibration of the field behavior at higher excitations using ^{3}He beams.

A momentum matching null method using a proton beam was used to establish an accurately known beam energy and reaction product magnetic

rigidity (Tr 70). This technique requires that the products of two reactions such as $^{12}C(p,p)^{12}C$ (elastic) and $^{12}C(p,d)^{11}C$ (ground state) be detected simultaneously at the spectrograph focal plane, and be induced by a beam of energy sufficient to give both reaction products equal outgoing magnetic rigidities. This beam energy is, of course, determined by the outgoing particle type, the scattering angle at which both are observed, and the Q-values of the reactions. For this pair of reactions with a $^{12}C(p,d)^{11}C$ Q-value of -16.4953 $\pm$ .0011 MeV (Ma 66) the beam energy is E_p = 33.691 $\pm$ .0022 MeV at θ_L = 15.0°. Furthermore, this beam energy is unique for a given pair of reactions, and the outgoing particle rigidity ($B\rho_p = B\rho_d$ = 332.256 Kg-in for this example) is unique as well. This situation is shown in Figure 2.2, where outgoing rigidities of the protons and deuterons are plotted as a function of beam energy. The point at which the curves cross determines the unique beam energy and magnetic rigidity value. It is of interest to note that the momentum match $B\rho$ value is quite insensitive to θ_L. Tables 2.1 and 2.2 list other reaction pairs and their Q-values suitable for momentum matching at other beam energies and magnetic rigidities. Figure 2.3 shows spectra of momentum matched protons and deuterons from the reactions $^{12}C(p,p')^{12}C(4.4398)$ and $^{12}C(p,d)^{11}C$ g.s. The spectra were taken simultaneously.

The accurately established $B\rho$ value and proton beam energy provide the vehicle for further calibrations. These reaction products may now be placed at a point on the spectrograph focal plane where all subsequent reactions are to be placed, and used to define an

effective radius of curvature for particles incident at that point. The relation is

$$\rho(\text{effective}) = \frac{B\rho\ (\text{momentum match})}{B_{NMR}}$$

where

$$B_{NMR} = \frac{\text{NMR frequency (MHz)}}{4.2577\ \text{MHz/KG}}$$

is the field value given by the NMR probe. The establishment of a unique beam energy and magnetic rigidity is independent of any measurement other than determining that both reactions are incident at the same focal plane position. This criterion was accomplished by adjusting the beam energy until the centroids of the proton and deuteron peaks coincided as seen via the position sensitive detector at the focal plane. The ability to discern when the centroids were coincident represents the experimental limit of the calibration, and previous work indicates that determining centroid differences to 0.1 mm or better is not unreasonable. Once a match had been established, it was checked by moving the peaks across the counter by changing the field. For a real match the centroids must remain coincident. A relative shift of centroids in this process indicates a spurious match, possibly caused by DC biasing of the detector pulses, or zero level shift in the ADC's.

For these proton reactions the scattering angle was measured using the reaction $^{1}H(p,p)^{1}H$ in a formvar foil of negligible thickness. The high kinematic spread of the scattered protons (298 KeV/deg at $\theta_L = 15.0°$) allowed measurement of the angle to ± 0.05. Since

the momentum matched beam energy is sensitive to the angle by the amount $\frac{dE(beam)}{d\theta(lab)}$ = 30 KeV/deg this required the original positioning of the spectrograph to be accurate to only $\pm$ 0.5°. The precise value of the scattering angle was then used to calculate the beam energy to 4 KeV or better.

Once a beam energy and ρ(effective) were defined by the momentum match, and the scattering angle measured, the spectrograph behavior at other field excitations were calibrated. This was accomplished by observing other reactions at the focal plane position defined by ρ(effective). These reactions are listed in Table 2.3. The magnetic rigidity of the outgoing particles of these reactions were calculated knowing the beam energy (the momentum match beam), the scattering angle, the target thickness and the reaction Q-values. These calculated rigidities were then compared to the rigidity measured in the spectrograph when the reaction products were placed at ρ(effective), namely:

$$B\rho(\text{experimental}) = B_{NMR} * \rho(\text{effective}).$$

The comparison of the calculated $B\rho$ values to those determined experimentally calibrates the spectrograph behavior at ρ(effective) for a given NMR reading. Several judicious points at various field excitations provided a calibration over the range of interest. The ratio $\frac{B\rho(\text{calculated})}{B\rho(\text{experimental})}$ was plotted against spectrograph NMR readings, and this calibration, is shown in Figure 2.4.

The upper curve represents two independent calibrations on separate days using the $^{12}C(p,p)^{12}C$ elastic and $^{12}C(p,d)^{11}C$ g.s. match and indicates the reproducibility of this data. The lower

curve is a third calibration using $^{12}C(p,p')^{12}C(4.4398)$ and $^{12}C(p,d)^{11}C$ (g.s.) The beam energy and Bρ value required for this second pair (E_p = 28.927 MeV, $B\rho_p = B\rho_d$ = 282.822 Kg-in at θ_L = 11.0°) defined a different value of ρ(effective) for the subsequent calibration and Q-value measurements. The reproducibility is again indicated by the fact that the curves are very nearly parallel. For both curves, several points were taken for each reaction on separate cycles of the magnet.

2.3 ^{3}He Beam and ^{6}He Energies

The ^{3}He beam energy for each run was determined by measuring the magnetic rigidity of ^{3}He elastic scattering from ^{12}C and ^{16}O. The procedure required adjusting the spectrograph field such that these elastic peaks were incident at the focal position defined by the momentum match. The rigidities of the elastically scattered ^{3}He were then calculated from the $\frac{B\rho(\text{calculated})}{B\rho(\text{experimental})}$ curve (Figure 2.4), the NMR frequency, and the value of ρ(effective). The relation is:

$$B\rho(^3\text{He}) = \frac{F(\text{NMR})}{4.2577} * \rho(\text{effective}) * \frac{B\rho(\text{calculated})}{B\rho(\text{experimental})}$$

This rigidity of the ^{3}He (hence the momentum and energy) plus knowledge of the scattering angle is sufficient to determine the beam energy.

When ^{3}He beams were used, the scattering angle was checked by measuring the reaction $^1H(^3He,^3He)^1H$ on a formvar foil. The outgoing ^{3}He energy was determined in the manner described above, and the angle determined from the reaction kinematics. The high kinematic spread of the ^{3}He (1490 KeV/deg for E = 68.5 MeV and θ_L = 11.0°) makes

the angle calculation very insensitive to the ^3He beam energy. A spectrograph entrance aperature of $\pm 0.08°$ was used for the angle measurements to reduce the energy spread acceptance and maintain reasonable peak shape. Figure 2.5 shows a sample position spectrum of the $^1H(^3He,^3He)^1H$ reaction.

Additional information on the spectrograph calibration was obtained by measuring the ^3He induced reaction shown in Table 2.4. Since the ^3He beam energy and scattering angle were known, and ρ(effective) previously defined, these reactions provided additional $\frac{B\rho\,(\text{calculated})}{B\rho\,(\text{experimental})}$ data. For this reason, these points are also displayed on the calibration curve (Figure 2.4).

The outgoing ^6He energies from the $^{12}C(^3He,^6He)^9C$, $^{16}O(^3He,^6He)^{13}O$ and $^{24}Mg(^3He,^6He)^{21}Mg$ reactions were measured in the same manner as the elastic ^3He. However, since the beam energy and scattering angle had been measured, the ^6He energies allowed the $(^3He,^6He)$ Q-values to be calculated.

During each ^3He run, data was taken for all calibrating reactions as well as $(^3He, ^6He)$ reactions on each cycle of the spectrograph field. In effect each such cycle provided an independent measurement of the desired Q-values.

2.4 Beam System

Beams for this experiment were prepared in the Michigan State University Sector-focus Cyclotron and delivered via the analysis and transport system (Ma 67). A general view of the experimental area is given in Figure 2.6. The slit boxes on the analysis system (S1, S2, S3)

were typically set to deliver a beam of maximum energy spread of $\pm$20 KeV at 70 MeV and maximum radial divergence of $\pm$2 milliradians. Magnets M3 and M4 provided the initial energy analysis, and M5 is a switching magnet. The direction of the beam incident on target was defined by two sets of slits S4 and S5. Slits S4 are current reading and are permanently located between the scattering chamber and last quadrupole, 85 inches from the center of the chamber. These slits were set at $\pm$0.30 inches from the beam line center.

Slits S5 are mounted on the target frame, and a $\pm$.030 inch opening defined the scattering chamber center and spectrograph object point. These slits were also current reading. After the beam had been aligned using M5 and M6, the S5 slits were lowered out of the beam and the targets were bombarded. Continuous monitoring of the slits S4, and the availability of monitoring S5 at any time assured constancy of incident beam direction. In addition, the switching magnet M5 was continuously monitored with an NMR.

The slits labled S6 are located at the entrance to the spectrograph 10.67 inches from the target, and define the solid angle. Three solid angle defining slits were used for this experiment; 1.2 msr subtending 2° in the scattering plane and 2° vertically, 0.30 msr subtending 1° in the scattering and 1° vertically, and 0.05 msr subtending 0.16° in the scattering plane and 1° vertically.

Most of the proton calibration work was done with the 1.0° slit since the cross sections were substantial, and minimum kinematic spread in the peaks was desired. This was necessary since the calibration work was done without moving the detecting apparatus to

compensate for kinematic spread. For the (^{3}He,^{6}He) reaction the large solid angle 2.0° X 2.0° slit was used.

A check with an optical surveyor's telescope verified that the centers of all three slits coincided. Also, as a check that no spurious effects arose in the placement of the reaction peaks at the focal plane due to slit changes, many of the calibrating reactions were observed with each of the three slits (at constant spectrograph field). No centroid shift was found to be significantly greater than the statistical error of the centroid itself.

2.5 Particle Detection and Identification

Particle detection and identification at the spectrograph focal plane was accomplished with a 300 μ position sensitive silicon surface barrier detector (Da 69 and Jo 70). The energy loss signals position signals were fed into separate Ortec Model 109 preamplifiers and from there into two Tennelec Model TC-200 amplifiers. These amplifiers were used in AC coupled, double differentiating mode to prevent DC biasing of the pulses. This is particularly important since the position information from the detector is computed as:

$$X(\text{position}) = X\Delta E \text{ pulse}/\Delta E \text{ pulse}$$

Thus, any constant added to one of the pulses (DC bias or raised zero level) would yield erroneous position information. The zero levels of the ADC's were also checked with a precision pulser before each run to eliminate offset zero levels. The amplifier operating time constants were .8 μsec. The amplified pulses were then sent

to two Northern Model NS-629 ADC's and hence to the Laboratory's XDS Sigma-7 computer where the data was analyzed on-line. Figure 2.7 is a diagram of the detector and electronics setup. The data taking routine TOOTSIE (Ba 69) displays the data according to the energy loss in and position along the detector. An example of this display is shown in Figure 2.8. The particles are incident on the detector at an angle of about 45° giving the detector an effective thickness of ~425 μ. Particles were identified via their differential energy loss in the detector. The detector was biased at -150 volts and cooled with alcohol at dry ice temperature.

2.6 Kinematic Compensation

Kinematic compensation requires that the energy spread across the spectrograph entrance aperature of the reaction products due to the reaction kinematics be refocussed at the detector, and not be observed in the peak width. The design of the spectrograph provides for a fixed focal plane for paraxial rays emerging from its object point in the scattering chamber. With a finite angular acceptance in the scattering plane, however, the energy difference between rays accepted at angles $\theta_L + \delta$ and $\theta_L - \delta$ due to kinematic spreading is not negligible (this energy spread would be 264 KeV for the 1.2 msr aperature and the $^{12}C(^{3}He,^{6}He)^{9}C$ reaction at 10°).

The effect is that the ray entering at $\theta_L - \delta$ has a higher energy, and traces a larger radius of curvature than the paraxial rays. The ray entering at $\theta + \delta$, being at a lower energy, traces a correspondingly shorter radius of curvature. The net effect is that these rays

intersect one another (focus) closer to the spectrograph than the paraxial rays do, and the focal point moves toward the spectrograph and becomes a circle of least confusion of rays. The equation used for calculating this shift (Δ) of the focal point is (Sp 67):

$$\Delta = [DM_H \rho K_\theta (T_i/T_o)^{1/2} \sin\theta] \; / \; [(K_o - K_\theta)(T_i/T_o)^{1/2} \cos\theta]$$

where: Δ = focal plane shift for a given reaction at radius of curvature ρ

D = spectrograph dispersion at ρ

ρ = radius of curvature

$K_\theta = (M_i M_o)^{1/2} / M_R$

M_i = mass of incident particle

M_o = mass of detected reaction product

M_R = mass of residual nucleus

$K_o = 1 + M_o/M_R$

T_i = energy of incident particle

T_o = energy of detected reaction product

θ = mean laboratory scattering angle

More complete discussions of this phenomenon may be found in references (Sp 67) and (En 58). For the (^{3}He,^{6}He) reactions measured here this focal shift was three to six inches at ρ = 32 inches.

The apparatus necessary to achieve this compensation consisted of a 50-inch plate or detector holder mounted on two motor operated drive screws in the spectrograph camera chamber. This allowed the detector holder to be driven horizontally toward the spectrograph exit port. The detector holder may also be driven vertically allowing the detector to be placed at the position of optimum count rate.

The relativistic kinematics calculations and computations of various spectrograph parameters were made with the computer program SPECTKINE. In addition to the reaction kinematics it provides NMR frequency and magnet decapot settings as well as calculations of the kinematic shift described above.

2.7 Cycling Effects

It has been observed that the spectrograph field behavior is sensitive to the field recycling procedure used (Sn 67). In particular, the calibration data showed that cycling at different speeds caused apparent changes in the effective field strength relative to a constant reading of the NMR frequency, This effect was made negligible by using a cycling time of 40 minutes for a field change of 0.0 to 0.9 to 0.0 of its maximum value. All data was taken on the 0.0 to 0.9 half of the cycle with the field always rising to its desired value.

Once the proper cycling procedure had been ascertained for the spectrograph, there was very little field drift as monitored by the NMR. Such fluctuations amounted to about $\pm$0.7 KHz (at a frequency of $\approx$55 MHz). This introduced an uncertainty in the outgoing ^{6}He energy of only $\pm$0.6 KeV.

2.8 Dispersion Matching

Partial dispersion matching was used to reduce the effects of beam intensity shift within the energy limits set by the beam transport-analysis system (especially important in three to six hour runs). A perfect match would mean that the energy dispersion of the beam

produced by the cyclotron and analysis system would be exactly compensated by the dispersion produced in the spectrograph. The net result of the ideal situation would mean a finite width (and energy dispersed) beam spot at the spectrograph target would be focussed to a point by the spectrograph. This is shown graphically in Figure 2.9. The effect of a total or partial dispersion match is reduced image width for a given reaction. In addition, the peak centroid is made less sensitive to fluctuation in the energy intensity pattern of the incident beam.

The dispersion matched condition was created by choosing quadrupole lens settings that gave the dispersed beam a width on target commensurate with that required by the dispersion characteristics of the spectrograph. The amount of dispersion match actually used in this experiment ranged from 50-75% of total match. The energy dispersion required by the spectrograph for perfect matching is:

$$\frac{\Delta X}{\Delta E} = \frac{D\rho}{2M_H E}$$

where $\frac{\Delta X}{\Delta E}$ is the energy dispersion of outgoing particles across the target, ρ is the radius of curvature at which matching is achieved, M_H is the horizontal magnification, and D the dispersion of the spectrograph at ρ and E is the mean energy of the outgoing particles.

2.9 Constant Radius of Curvature

The success of accurate energy measurements in the spectrograph depends upon defining an effective radius of curvature (or a corresponding focal plane position), and placing all pertinent reaction products

there. Since the information regarding the peak positions was obtained through detector pulses analyzed by computer, and consequently appeared to change with changes in amplifier gains or ADC conversion gains, some method of providing a fiducial mark at the focal plane was required. This requirement was filled by mounting a collimated ^{241}Am alpha source on the counter bench unit one inch from the counter. The counter could then be lowered vertically in its bench to the level of the source. The resulting alpha peaks then provided a positive position indicator on the counter with a corresponding position channel number. When the amplifier gains were changed, it was a simple matter to lower the detector and recalibrate. Figure 2.10 shows photographs of the focal plane apparatus, alpha source, and detector. Figure 2.11 shows the three resulting calibration alpha peaks.

The alpha source also provided an energy calibration for the counter since the alpha group energies are well known (5.48 MeV for the dominant group). Thus particle energy loss in the detector and electronic noise level could be calibrated without recourse to a pulser.

Since it is also critical that the detector not be moved relative to the alpha source between the proton calibration and the taking of (^{3}He,^{6}He) data, each run consisted of both a proton calibration and ^{6}He data taking without removing the detector or its mount from the camera chamber.

The alpha source, however, moved with the detector when the focal plane apparatus was moved to compensate for kinematic spreading. To insure that the radius of curvature defined by the proton calibration intersected the same point on the focal plane despite this movement,

the elastic ^{3}He from ^{12}C were observed at this point as the detector was moved to various positions. The result was a calibration for the drive screws in which the ^{3}He peak centroid always maintained its proper position. The $\pm 0.08°$ entrance slit was used for this calibration to minimize the peak widths and maintain good peak shape.

Table 2.1 Some Useful Reactions for Calibration in Momentum Matching Method

Reaction	Ex(Residual Nucleus) MeV±KeV	Q-value
$^{12}C(p,p)^{12}C$	0.0	0.0
$^{12}C(p,p)^{12}C^*$	4.4398±0.3[a]	-4.4398±0.3
$^{16}O(p,p)^{16}O$	0.0	0.0
$^{16}O(p,p)^{16}O^*$	6.1305±0.4[b]	-6.1305±0.4
$^{12}C(p,p)^{11}C$	0.0	-16.4953±1.1[d]
$^{16}O(p,d)^{15}O$	0.0	-13.4434±1.2[d]
$^{16}O(p,d)^{15}*$	6.180±4.0[c]	-19.6234±4.0

[a] See (Ch 67)

[b] See (Mar 67)

[c] See (Wa 65)

[d] See (Ma 66)

Table 2.2 Possible Reaction Pairs for Momentum Match Energy Calibrations
Calculations are for $\theta_L = 15.0°$

Reaction 1	Excitation Energy 1 (MeV±KeV)	Reaction 2	Excitation Energy 2 (MeV±KeV)	Beam Energy (MeV±KeV)	Beam Particle	Magnetic Rigidity of Outgoing Particles (Kg.in)
$^{12}C(p,p)^{12}C$	0.0	$^{12}C(p,d)^{11}C$	0.0	33.691±2.2	P	332.256
$^{12}C(p,p)^{12}*$	4.4398±.3	$^{12}C(p,d)^{11}C$	0.0	29.009±2.2	P	282.884
$^{16}O(p,p)^{16}O$	0.0	$^{16}O(p,d)^{15}O$	0.0	27.336±2.5	P	299.009
$^{16}O(p,p)^{16}O$	0.0	$^{16}O(p,d)^{15}O^*$	6.180±4.	40.106±8.	P	363.381
$^{16}O(p,p)^{16}O^*$	6.1305±.4	$^{16}O(p,d)^{15}O$	0.0	20.981±2.5	P	219.312
$^{16}O(p,p)^{16}O^*$	6.1305±.4	$^{16}O(p,d)^{15}O^*$	6.180±4.	33.607±8.	P	299.600

Table 2.3 Spectrograph Calibrating Reactions for Proton Beams

Reaction	Excitation Energy (MeV±KeV)	Q-value $Q_o + E_{EXC}$ (MeV±KeV	Outgoing Rigidity (Bρ) For E(BEAM) = 33.691 θ_L = 15.0°
$^{12}C(p,p')^{12}C^*$	4.4398±0.3	-4.4398±0.3	309.085
$^{16}O(p,p')^{16}O^*$	6.1305±0.4	-6.1305±0.4	300.064
$^{16}O(p,d)^{15}O$	0.0	-13.4434±1.2	361.263
$^{27}Al(p,d)^{26}Al$	0.0	-10.8322±2.9[a]	384.616
$^{7}Li(p,d)^{6}Li$	0.0	-5.0280±1.6[a]	425.142
$^{7}Li(p,d)^{6}Li^*$	2.184 ±2.0[b]	-7.212 ±3.0	409.201
$^{1}H(p,p)^{1}H$	0.0	0.0	

[a] See (Ma 66)

[b] See (Aj 66)

Table 2.4 Spectrograph Calibration Reactions for ^{3}He Beams

Reaction	Excitation Energy (MeV ± KeV)	Q-value ($Q_o + E_{EXC}$)	Outgoing Rigidity (Bρ) for E(BEAM)=68.500 MeV θ_L = 11.00°
$^{12}C(^{3}He,^{3}He')^{12}C^*$	4.4398±0.3	-4.4398±0.3	394.168
$^{16}O(^{3}He,^{3}He')^{16}O^*$	6.1305±0.4	-6.1305±0.4	389.305
$^{12}C(^{3}He,^{3}He)^{12}C$	0.0	0.0	407.902
$^{16}O(^{3}He,^{3}He)^{16}O$	0.0	0.0	408.385
$^{12}C(^{3}He,^{4}He)^{11}C$	0.0	1.8582±.0012[a]	473.490
$^{13}C(^{3}He,^{4}He)^{12}C$	0.0	15.6312±.0009[a]	516.704
$^{16}O(^{3}He,^{4}He)^{15}O$	0.0	4.9101±.0013[a]	484.592
$^{1}H(^{3}He,^{3}He)^{1}H$	0.0	0.0	

[a] See (Ma 66)

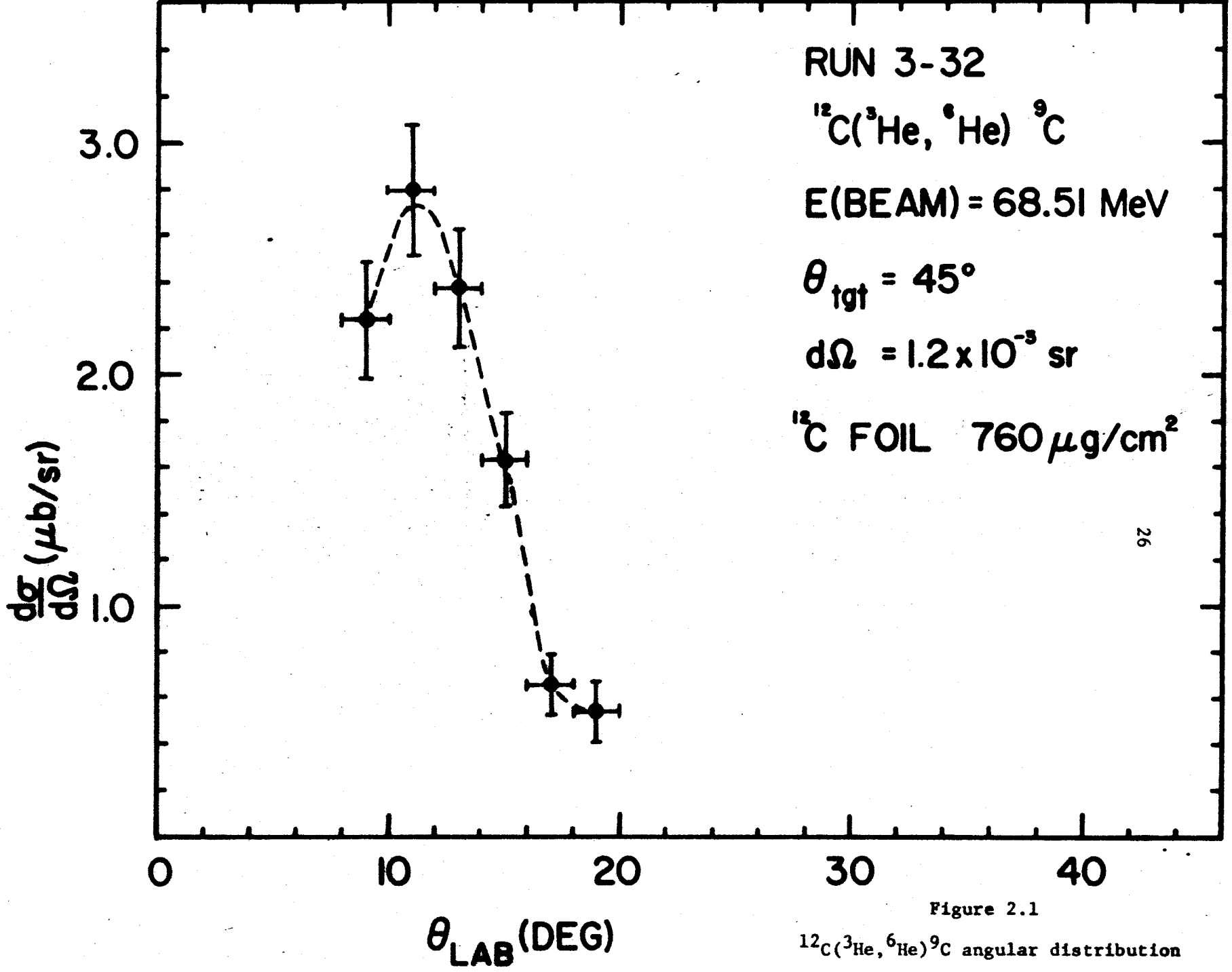

Figure 2.1

$^{12}C(^{3}He, ^{6}He)^{9}C$ angular distribution

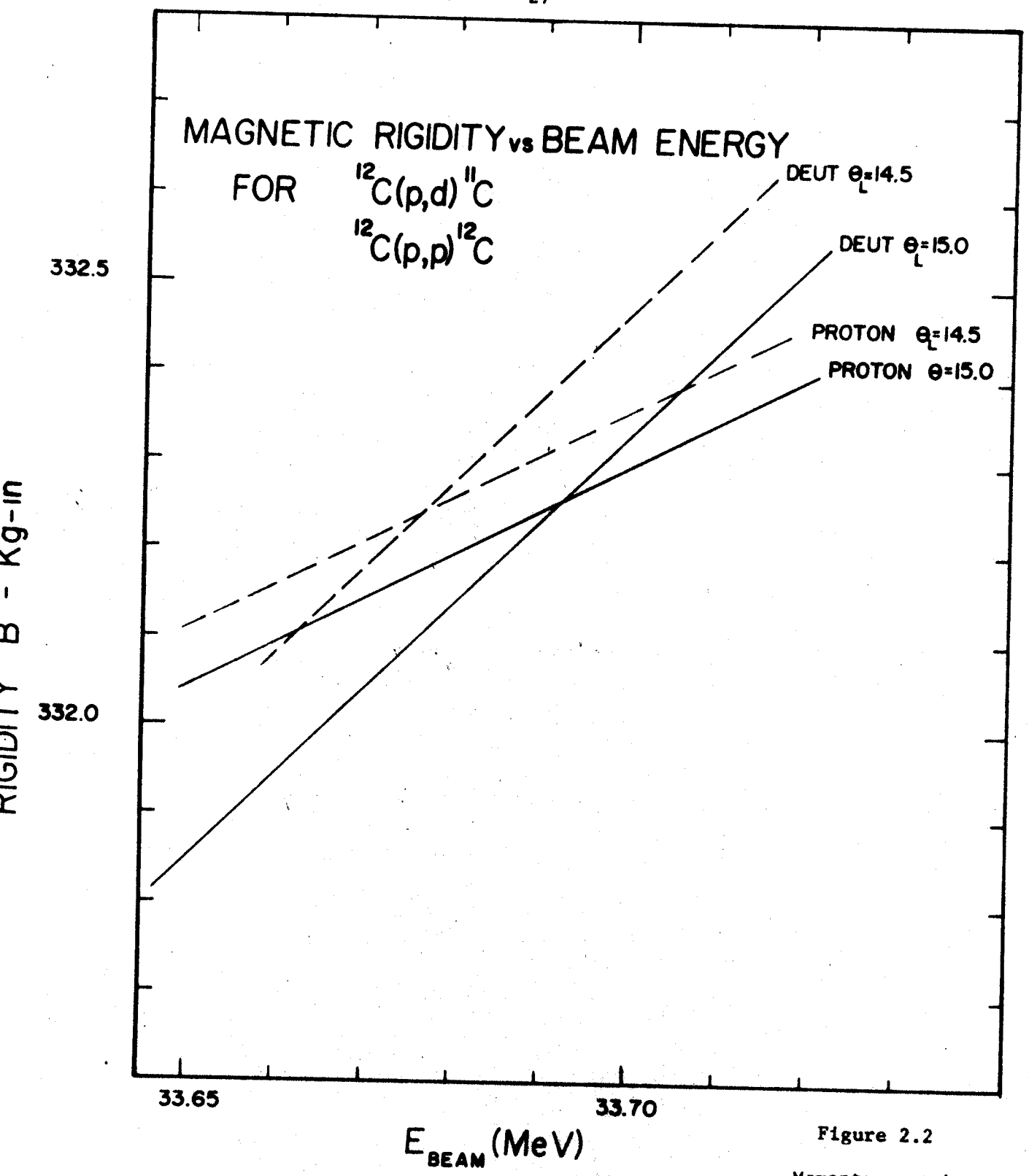

Figure 2.2

Momentum match

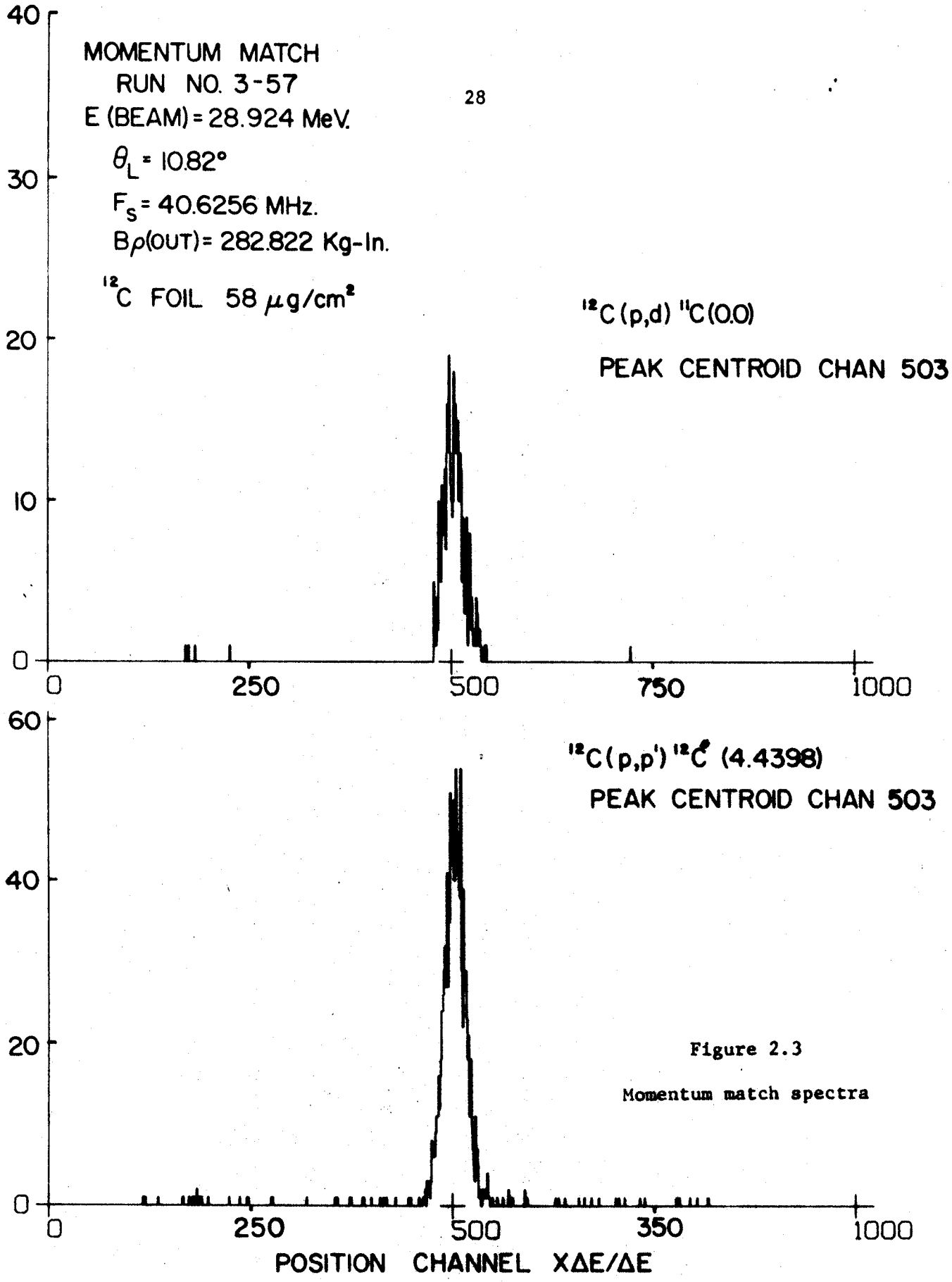

Figure 2.3

Momentum match spectra

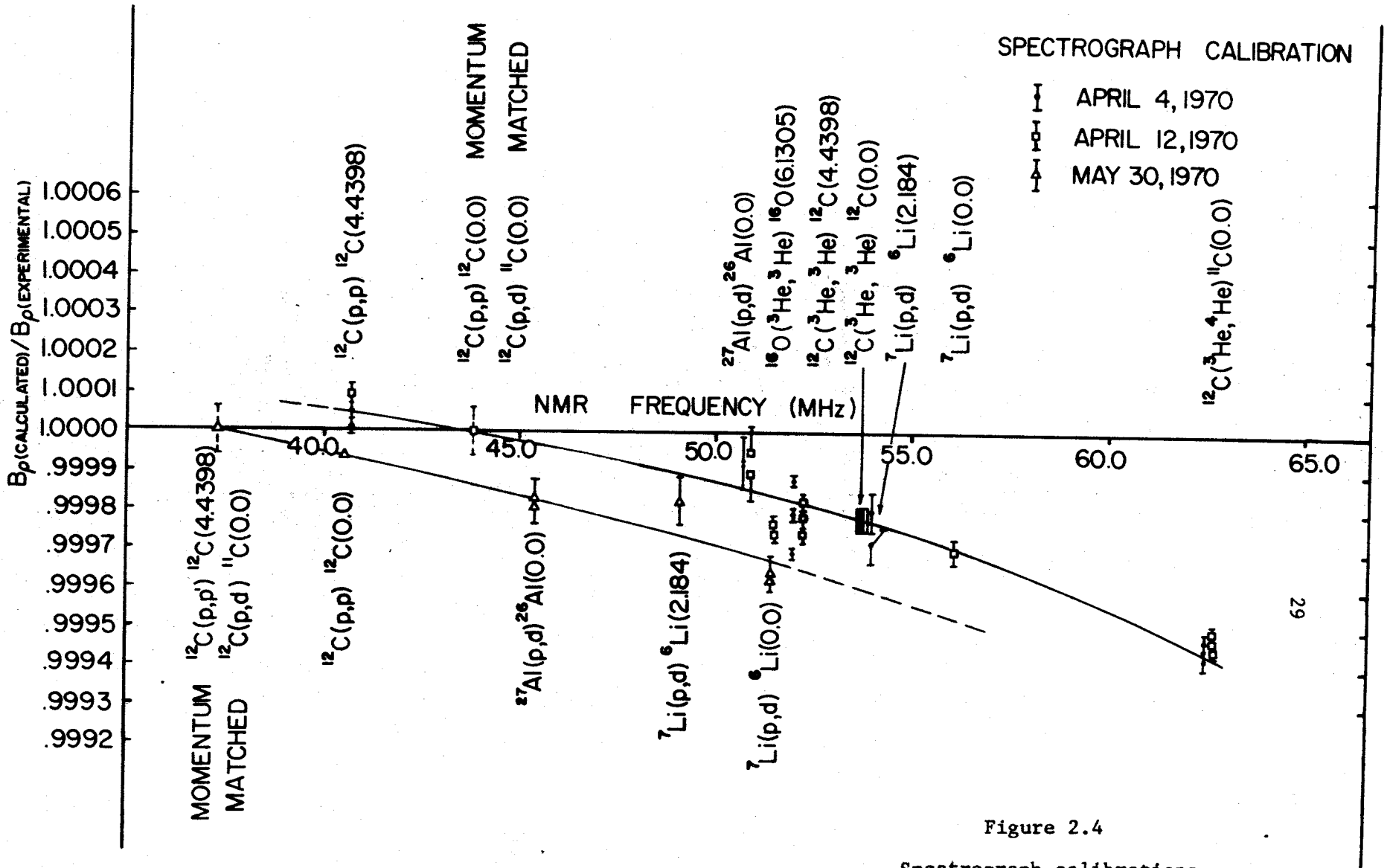

Figure 2.4

Spectrograph calibrations

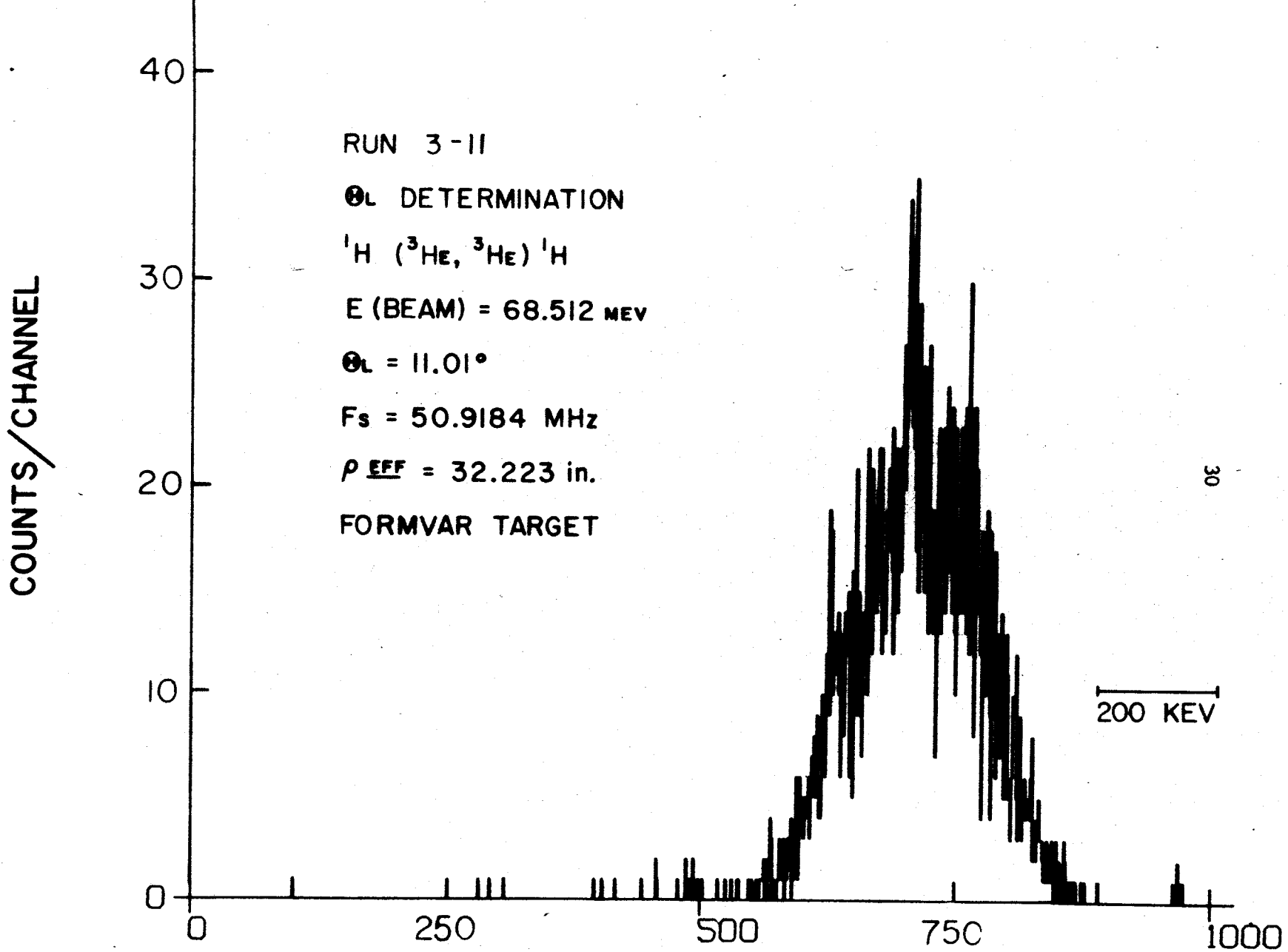

Figure 2.5
$^{1}H(^{3}He,^{3}He)^{1}H$ spectrum

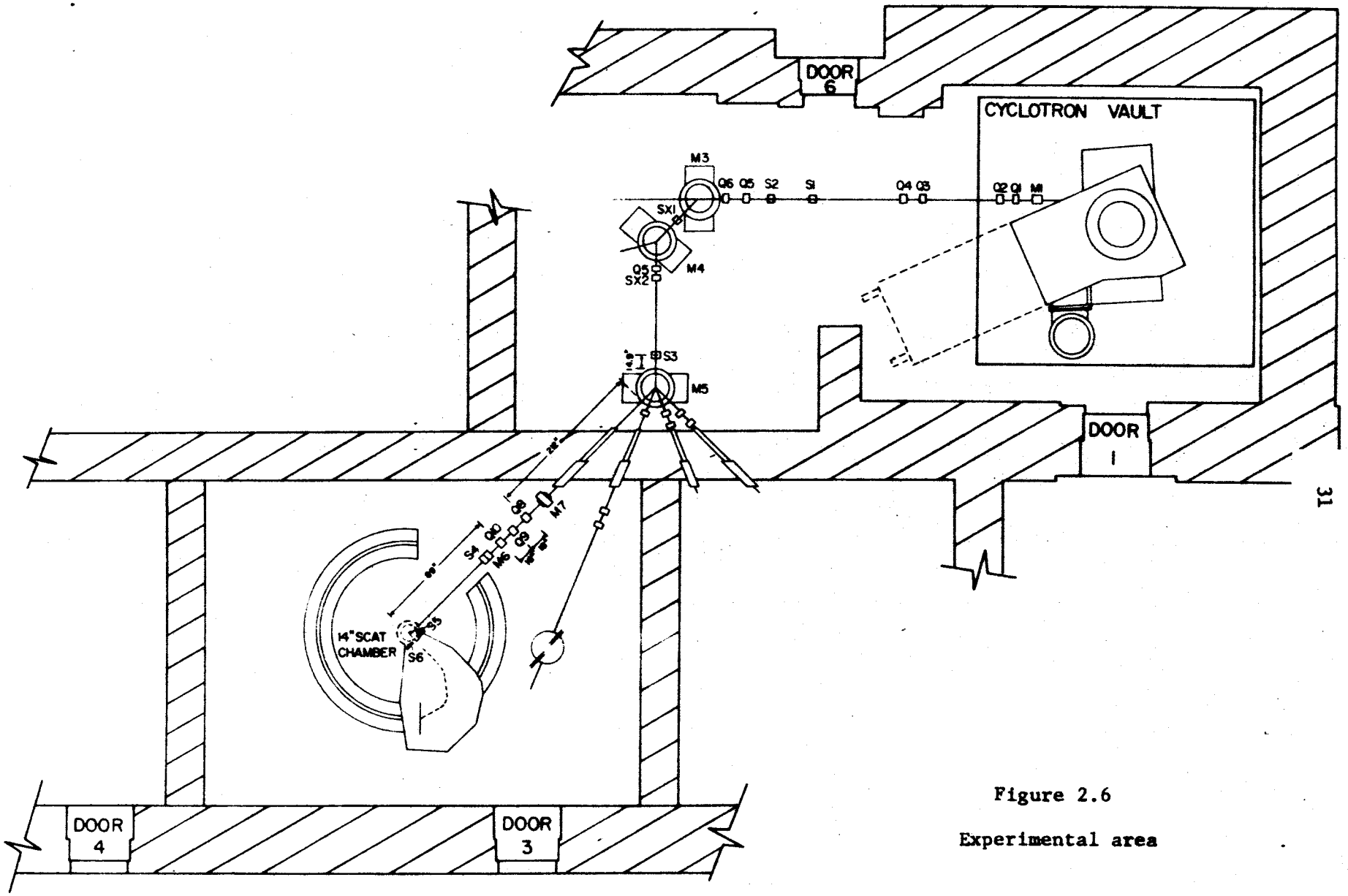

Figure 2.6

Experimental area

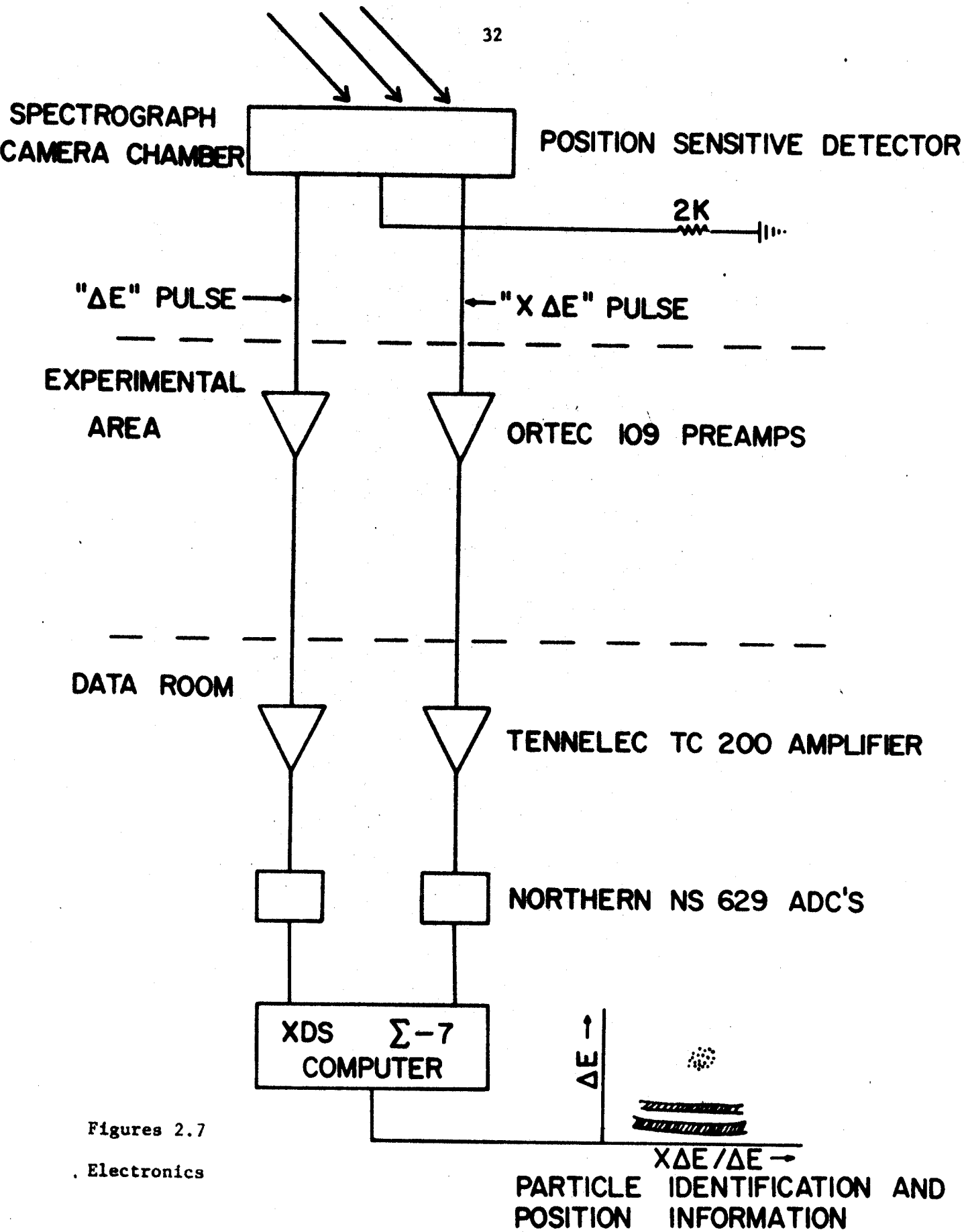

Figures 2.7

. Electronics

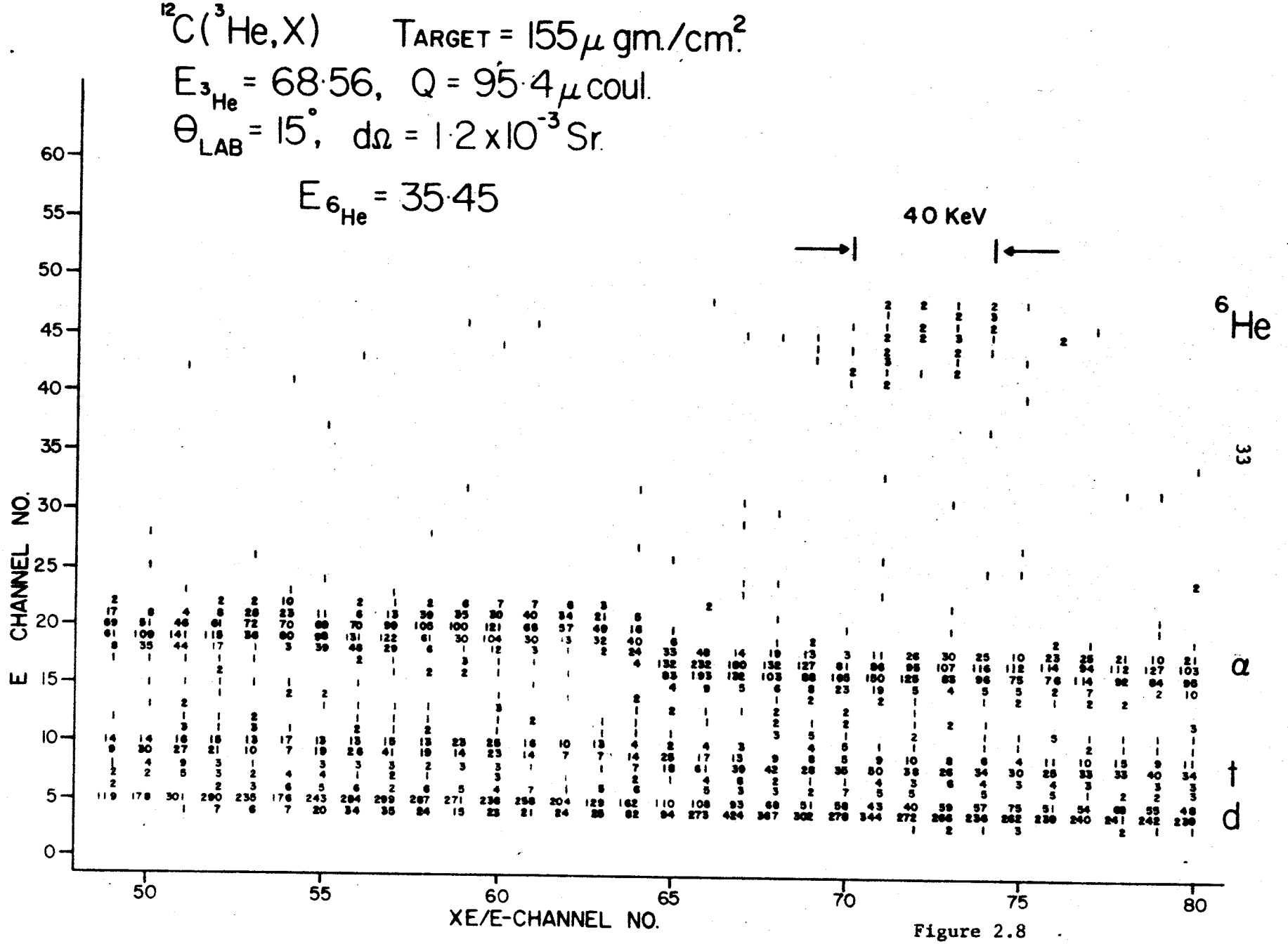

Figure 2.8

Particle identification spectrum

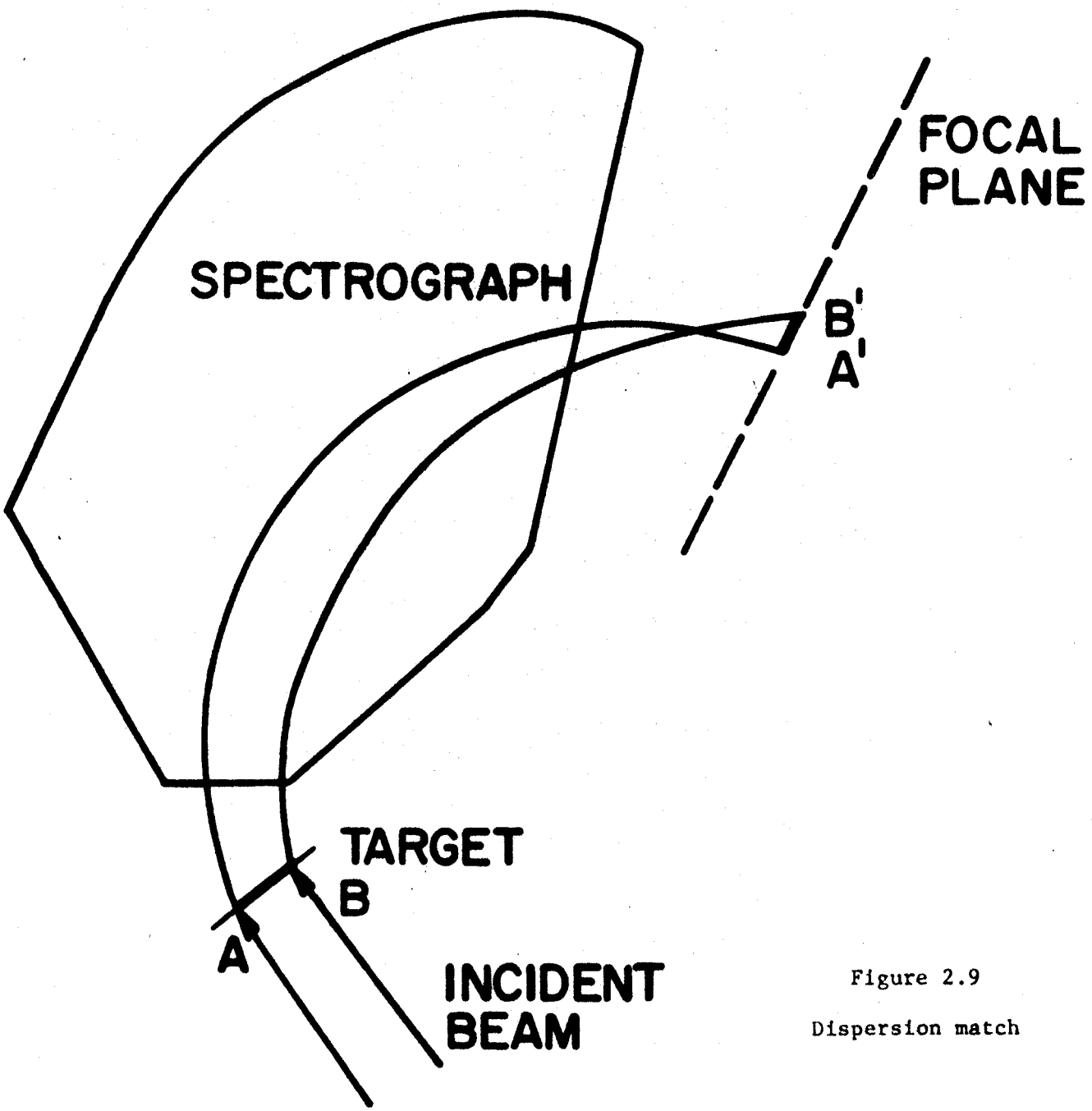

Figure 2.9

Dispersion match

If the beam energy increases from B to A, the spectrograph dispersion reduces image width B'A'

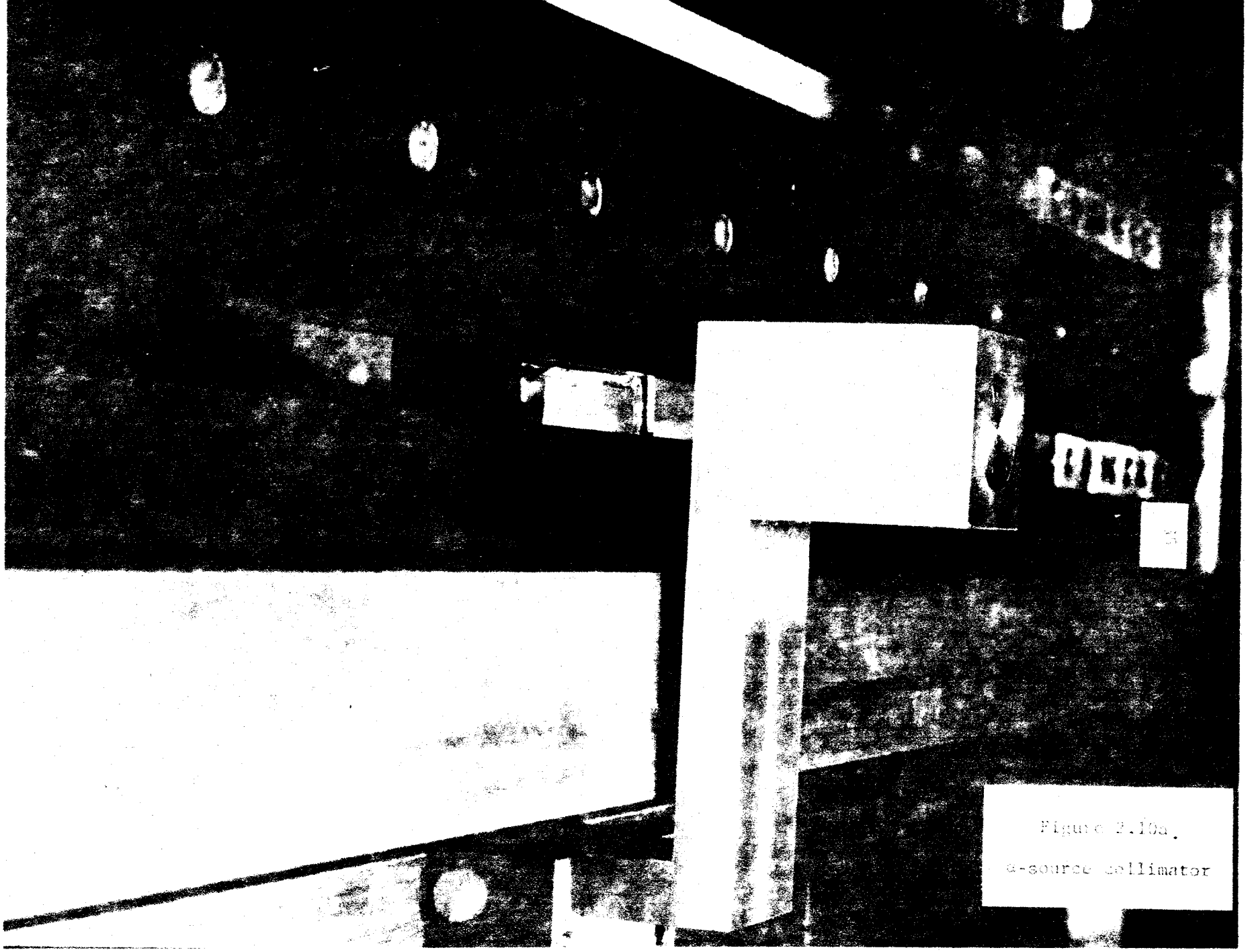

Figure 3.10a.
α-source collimator

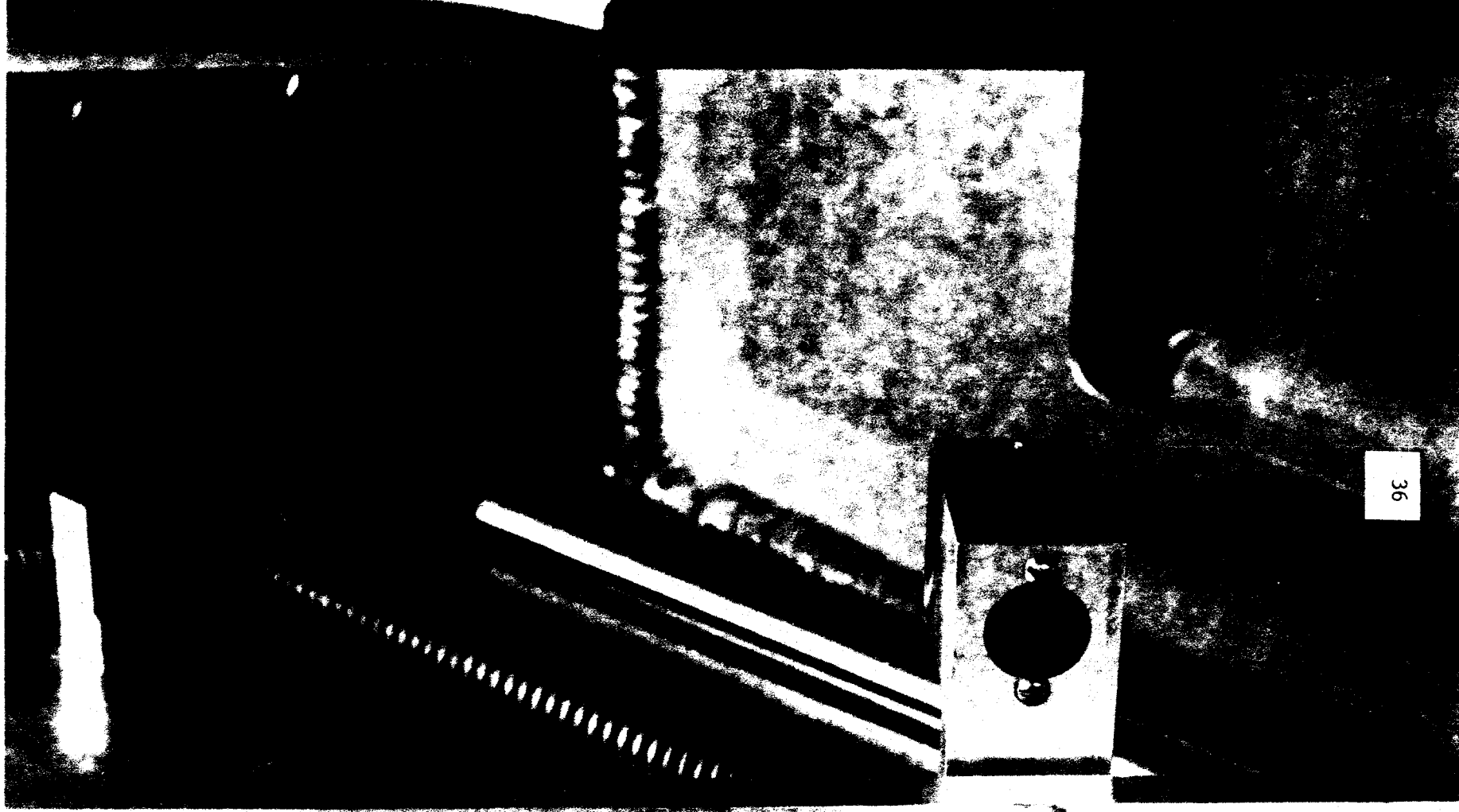

Figure 2.10b

α-source collimator

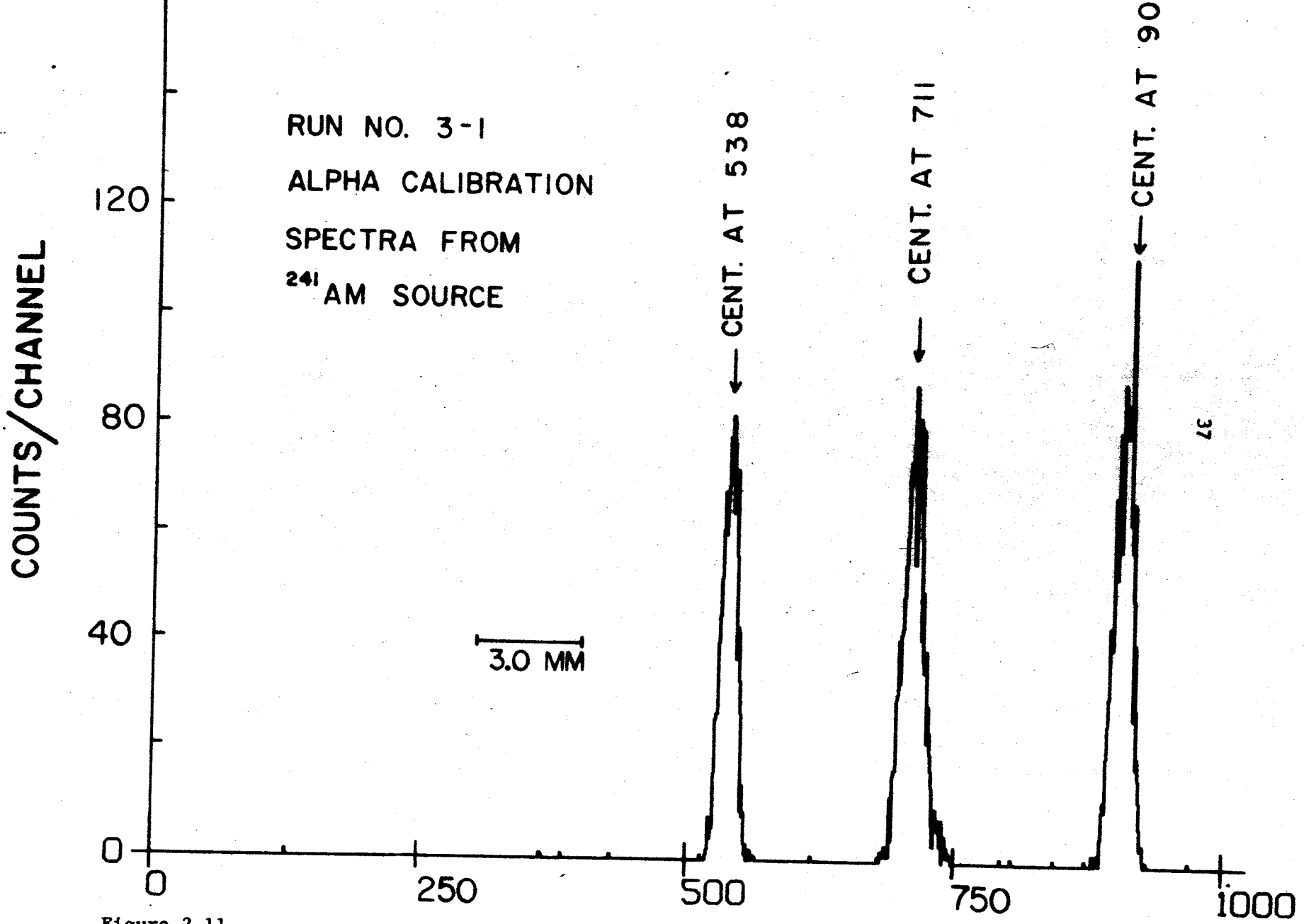

Figure 2.11

Position calibration spectrum

2.10 Target Thickness Measurements

The ^{3}He and ^{6}He energy loss in the targets used in this experiment represent a significant correction to the measured outgoing ^{6}He energies, and therefore, careful measurement of all targets was required. The targets were measured in air with an alpha source gauge, and the energy losses for various particles calculated using the published tables (Wia 66). The appropriate ^{6}He loss was taken to be that of a ^{3}He at half the ^{6}He energy.

Briefly, the measuring technique requires passing 5 MeV α-particles from an ^{241}Am source through the target (located a fixed distance from the source) and detecting them with a solid state detector mounted on a micrometer. When the total thickness of air and target material between the source and counter is not sufficient to stop the alphas, the count rate measured at the detector will be essentially constant. As the counter is moved away from the source, however, the alphas begin stopping before reaching the detector. In this region, the count rate falls rapidly to zero as the counter is moved further away, and the micrometer reading gives this distance quantitatively. The target is then removed and the measurement repeated with only air between the counter and source. This produces a curve similar to the first, but displaced from it a distance equal to the air equivalent thickness of the target material for the alphas. Figure 2.11 shows the data of such a measurement for a ^{12}C foil.

Knowing the air pressure and temperature allows a calculation of the density of, and hence the alpha energy loss through the air

(or equivalently, through the target). This in turn allows the target thickness in mg/cm^2 to be calculated. Several measurements were made over the surface of each target foil to obtain an average thickness value. It may be noted also that since target thickness is measured relative to an equivalent amount of air, precise knowledge of the alpha energy used is not critical if the stopping power of the target elements are commensurate with that of air.

Once the target thickness and desired energy losses were established, they were applied as corrections to the outgoing particles as follows:

$$\overline{\Delta E}_{LOSS}(\text{outgoing}) = 1/2[\Delta E_{LOSS}(\text{outgoing}) + \Delta E_{LOSS}(\text{incident})]$$

This assumes that on the average the desired reaction will occur at the target center, and consequently both the incident beam particles and reaction product will be reduced in energy by half the target. The average energy loss for the outgoing particles in the target was then introduced as an effective excitation energy in the corresponding reaction kinematic calculations.

The uncertainty in the energy losses was estimated by making several separate measurements of each target. Table 2.5 lists all targets used for this experiment, their thickness in mg/cm^2, the average energy loss of ^6He (as described above) and the uncertainty in the energy loss.

Table 2.5 Targets Used For (^{3}He,^{6}He) Reactions

for E(BEAM) = 68.0 MeV

Targets	Thickness(mg/cm^2)	E(^{6}He), Ave. Loss(KeV)
^{12}C #1	0.153	25.4±3
S_{10}, F-80	0.227	34.1±4
"Glass" S_iO_2	0.491	71.0±8
^{24}Mg Foil	0.656	83.5±13
S_iO + C	0.432	66.5±7
^{12}C "F"	0.117	19.0±3

TARGET

DATE 5 - 30 - 70

PRESSURE 30.9 in. Hg

TIME 40 SEC.

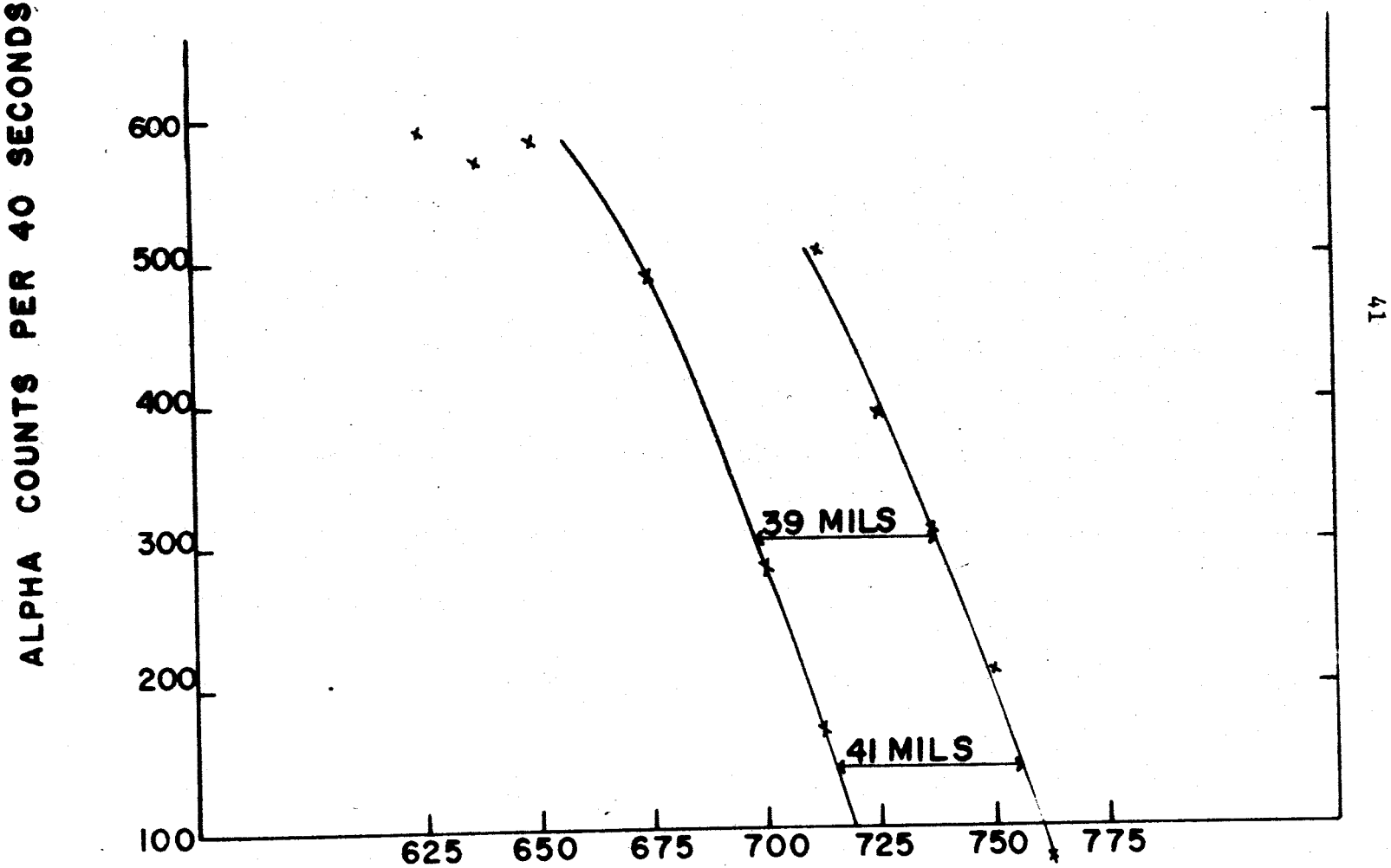

Figure 2.12

Target data

3. DATA ANALYSIS

Many of the parameters involved in obtaining the (^{3}He,^{6}He) Q-values were subject to experimental uncertainties that were difficult to determine quantitatively. Because of this, and because the goal of this experiment was precise measurement, several independent measurements were made. Beam energies and scattering angles were varied, and for the ^{9}C and ^{13}O measurements, several different targets were used. In addition, two different detector geometries were used; the first with particles incident at 45° in which the detector operated in the $\frac{dE}{dx}$ mode, and the second with particles incident at 53° and the detector operating in the E mode for the ^{12}C(^{3}He,^{6}He)^{9}C and ^{16}O(^{3}He,^{6}He)^{13}O reactions. Rotating the detector 8° relative to the incident particles also increased the effective energy dispersion across it by about 20%. Each of these independent runs was preceded by its own proton calibration run. In all, three such independent runs were made, and several measurements of the Q-values were taken during each run. These measurements made during each run were, however, subject to any systematic uncertainties in the preceding proton calibration run, in the detector geometry and in target thickness measurements.

Each Q-value determination was assigned an uncertainty consisting of all known parameter fluctuations summed in quadrature. For a particular measurement this would include beam energy fluctuation, scattering angle fluctuations, statistical error of the peak centroid, uncertainties involved in correcting peak centroids not falling

exactly on the focal point defined by ρ(effective), and any observed magnetic field fluctuations. A weighted average of all Q-value measurements for a reaction was then taken, with the weighting factors taken as the square of the uncertainty of each point. Since these uncertainties were very nearly the same for each point, the weighted average was numerically equal to an unweighed average for each reaction. In addition, the uncertainty of the average was computed using the same weighting factors according to the formula (Be 57)

$$\sigma^2 = \{\sum_i (W_i S_i)^2\}^{1/2} / \sum_i W_i$$

σ = error of average
W_i = weighting factor
S_i = error of point

The systematic uncertainties such as those assigned to the calibration procedure, and to target thickness measurements were then summed in quadrature, and added to the uncertainty of the average Q-value.

To check the validity of this assignment of uncertainties, the standard deviation of the distribution of individual measurements was also computed for each reaction. (For ^{9}C there were eight measurements, nine for ^{13}O and four for ^{21}Mg). In each case the standard deviation of the distribution and the total experimental uncertainty described previously were very nearly equal.

Finally, in computing the mass excesses of ^{9}C, ^{13}O, and ^{21}Mg, the uncertainties of the other masses involved, ^{3}He, ^{6}He, ^{12}C, ^{16}O and ^{21}Mg were also summed with the Q-value uncertainty in quadrature. The uncertainty of $\pm$ 4 KeV associated with the ^{6}He mass excess (Ma 66) was not negligible in computing the total error of ^{9}C and ^{13}O. The masses of ^{3}He, ^{6}He, ^{12}C, ^{16}O, and ^{24}Mg are given in Table 3.1.

Table 3.1 Mass Excesses of (^{3}He,^{6}He) Reaction Members (Ma 66)

Element	Mass Excess(MeV)
^{12}C	0.0
^{16}O	4.7365±.0003
^{24}Mg	-13.9333±.0017
^{3}He	14.9313±.0002
^{6}He	17.598 ±.004

4. EXPERIMENTAL UNCERTAINTIES

4.1 Uncertainties of Spectrograph Field Calibrations

Uncertainty in the field calibration curve (Figure 2.4) ($\frac{B\rho calc}{B\rho exp}$ curve) is the consequence of two separate phenomena; first the uncertainty in the $^{12}C(p,d)^{11}C$ Q-value since this reaction is used for the momentum match, and second the uncertainty of fit of the calibration curve to the calibrating reactions. These points will be dealt with separately.

Uncertainty Due to Momentum Match

As pointed out in the section on spectrograph calibration, the momentum match defines both a proton beam energy and an effective radius of curvature. Since it is such a point of definition, any calibration curve must necessarily pass through it regardless of where other related calibration points may lie. This momentum match beam energy has a minimum uncertainty of $\pm$ 2.2 KeV due to the 1.1 KeV uncertainty in the $^{12}(p,d)^{11}C$ Q-value. Since the calibration curve is required to pass through the point itself and since this beam energy is used in calculating the other calibration points, the effect of this 2.2 KeV uncertainty is to make any curve through the 2.2 KeV error bar acceptable as long as such a curve is parallel translation of the curve best fitting all of the calibration data. In other words, the location but not the shape of the calibration curve may be altered

by the uncertainty of the $^{12}C(p,d)^{11}C$ Q-value. This effect represents a systematic uncertainty in any outgoing particle rigidity (and hence outgoing energy) based on this curve; outgoing ^{3}He for beam energy and angle measurements, and outgoing ^{6}He, for example.

Quantitatively, the effect is the following. Since a translation of the calibration curve is reflected directly in outgoing particle energies:

$$\frac{\Delta E(\text{outgoing})}{E(\text{outgoing})} = \frac{2.2 \times 10^{-3}\ \text{MeV}}{33.691\ \text{MeV}}$$

where 33.691 MeV is the momentum match beam energy at $\theta_L = 15.0°$. This reduces to:

$$\Delta E(\text{outgoing}) = 6.7 \times 10^{-5} \times E(\text{outgoing})$$

for a ^{3}He beam E(BEAM) = 68.520 MeV producing a ^{6}He of E(^{6}He) = 36.069 the individual uncertainties would be $\Delta E(BEAM) = 4.7$ KeV and $\Delta E(^{6}He) = 2.5$ KeV. However, since any such systematic uncertainty must work in the same direction for both measurements, the uncertainty in the calculated Q-value is again their difference:

$\Delta Q = \Delta E(BEAM) - \Delta E(^{6}He) = \pm 2.2$ KeV for the parameters given above.

Uncertainty Associated With Calibration Curve

The uncertainty associated with the fit of the calibration curve to the calibrating reactions is basically an estimate. To make this curve as reliable as possible, an attempt was made to use calibrating reactions whose Q-values carried minimal experimental uncertainties.

The best of these (in this respect) are the $^{12}C(p,p')^{12}C$ (4.4398) (Ch 67) and the $^{7}Li(p,d)^{6}Li$ (g.s.) (Ma 66) reactions, as well as the momentum match point which falls between them. Fortunately these reactions span a rigidity region that includes the points required for determining the ^{3}He beam energy and the ^{6}He energies from ^{9}C and ^{13}O. The ^{3}He induced calibrating reactions $^{12}C(^{3}He,^{3}He')^{12}C(4.4398)$ and $^{12}C(^{3}He,^{4}He)^{11}C$ (using a ^{3}He beam energy determined via the proton calibration curve) then provided a check on the consistency of the curve shape over a greater rigidity range, particularly to that rigidity value required by ^{21}Mg. Using the quoted uncertainties of the calibration reaction Q-values, and considering the consistency of the curve shape over several sets of experimental measurements it is estimated that the uncertainty associated with the fit of the calibration curve is not greater than 0.5×10^{-4} of the outgoing particle energy. This uncertainty was applied directly to the outgoing ^{6}He energies and hence to the calculated Q-value. Quantitatively it amounted to about $\pm$ 2 KeV.

$$\Delta Q(\text{fit}) \leq 0.5 \times 10^{-4} \times E(\text{outgoing } ^{6}He) = 2.0 \text{ KeV}$$

4.2 Extrapolation to Defined Radius of Curvature

The essence of these Q-value measurements was choosing a spectrograph field that places the desired reaction at a very carefully calibrated point on the focal plane. Since in practice this was almost impossible to do exactly for the $(^{3}He,^{6}He)$ reaction (primarily because the low count rates did not always allow a great deal of time

for such fine tuning), some method of extrapolating from the actual particle group position to the desired position was required. The approach was the following: knowing the field and where the particles are, what would the field be if the particle group were where it belonged? Such a problem depends basically on two factors; the characteristics of the detector and the dispersion of the spectrograph. Since the dispersion is essentially constant, particularly over the length of the focal plane subtended by the detector (30 mm) (Sp 67), the relation between a peak centroid in some position channel C1 (or equivalently at some place on the counter analyzed as channel C1) with NMR frequency F1 and an equivalent centroid in channel C2 with frequency F2 is

$$\frac{F1 - F2}{(C1 - C2)\ \frac{(F1 + F2)}{2}} = \text{constant}$$

This is actually a statement of constant dispersion and should hold for a given detector geometry. In principle this constant may be calculated by taking some reaction such as $^{12}C(^{3}He,^{3}He)^{12}C$ and placing the peak in two different channels by changing the field and using the formula above. This constant and the formula would then allow determination of the field value that any other peak would have at ρ(effective).

Complications arise, however, due to nonlinearities in the detector response. This situation effectively makes the dispersion appear nonlinear. In order to calibrate for this effect, the detector was carefully mapped with one of the calibrating reactions (usually elastic

^{3}He from ^{12}C) during each run. This essentially yielded a set of dispersion "constants" for various areas of the counter. This information permitted subsequent mounting of the detector so as to utilize its most linear region. Doing so minimized nonlinearities to the point where an average value of the dispersion constant could be calculated over the region of interest. Since the dispersion is viewed via the detector and related electronics, it appears to depend upon the amplifier gains. The constant was, therefore, redetermined after any gain change.

The values of the dispersion constant for any given setup would vary by approximately 10% over the detector range of interest. Subsequently any such extrapolation of the field was given an uncertainty of 10% of the extrapolated value. Such extrapolations were generally in the range of 5-15 KHz, and all but two were less than 25 KHz. At an extrapolation of 25 KHz the uncertainty introduced is ± 2.5 KHz which translates into an uncertainty of ± 3.5 KeV in the outgoing ^{6}He energy (≈37 MeV).

The energy uncertainty was calculated as follows: for a given frequency interval ΔF at some average frequency F determining outgoing particle energy E(^{6}He)

$$\frac{2\Delta F}{F} = \frac{E}{E}$$

$$\Delta E = \frac{2\Delta F\ E}{F}$$

Therefore, for dispersion constant = $\frac{\Delta F}{F\Delta C}$ with uncertainty

$\delta\left(\frac{\Delta F}{F\Delta C}\right) = 10\% \frac{\Delta F}{F\Delta C}$ the Q-value uncertainty becomes

$$\Delta Q(\delta) = 10\% \times \frac{\Delta F}{F} \times 2 \times E = 0.20 \times \Delta F \times E(^6\mathrm{He}).$$

4.3 Peak Location

The uncertainty of the location of a peak centroid due to its shape and statistics was accounted for by calculating the statistical uncertainty of the centroid. For a peak with calculated centroid at C, the expression for C is

$$C = \sum_i n_i c_i \; / \; \sum_i n_i$$

where n_i is the number of counts in channel c_i,

and its uncertainty is

$$\delta C = \left[\sum_i n_i (c_i - C) \; / \; N(N-1)\right]^{1/2}$$

where N is the total number of counts in the peak

Translating this to energy units is accomplished as follows: for a centroid with uncertainty δC located at a detector position where the dispersion constant = $\frac{\Delta F}{F\Delta C}$, δC becomes an effective field uncertainty:

$$\delta F = \delta C \times \frac{\Delta F}{F\Delta C} \times F$$

and hence an uncertainty in the outgoing ^{6}He energy:

$$E(^6\mathrm{He}) = \delta C \times \left(\frac{\Delta F}{F\Delta C}\right) \times F \times 2 \times E(^6\mathrm{He})$$

In the majority of cases the centroid uncertainty ranged between 0.2 - 0.7 channels. For the typical value $\frac{\Delta F}{F\Delta C} = 1.5 \times 10^{-2} \frac{\text{KHz}}{\text{MHz channel}}$

this yielded uncertainties in the outgoing ^{6}He energies of 2.0 - 7.0 KeV. These uncertainties are reflected directly in the calculated Q-values:

$$\Delta Q(\delta C) = \delta C \times \left(\frac{\Delta F}{F \Delta C}\right) \times F \times 2 \times E(^6\text{He})$$

4.4 Scattering Angle Fluctuations

The uncertainty of outgoing ^{6}He energies due to uncertainties in the scattering angle θ_L consists of two parts. The first is a random contribution to each point due to possible fluctuation in beam direction while a particular data point was being taken. From consideration concerning the geometry of the beam delivery system and the general consistency of the calibration data this effect was estimated to yield an uncertainty in θ_L of ± .03°. This is reflected in the outgoing ^{6}He energy through the value of the kinematic energy spread for each reaction. Table 4.1 shows these values and the energy uncertainty for each reaction for θ_L = 11.00° ± .03° and E(BEAM) = 68.5 MeV.

Table 4.1. Uncertainty of Outgoing ^{6}He Energy for θ_L = 11.00° ± .03° and E(BEAM) = 68.5 MeV

Reaction	$^{12}C(^3He,^6He)^9C$	$^{16}O(^3He,^6He)^{13}O$	$^{24}Mg(^3He,^6He)^{21}Mg$
Kinematic Spread	150 KeV/deg	108 KeV/deg	70 KeV/deg
$E(^6He)$ for $\Delta\theta$=±.03°	± 4.5 KeV	± 3.3 KeV	± 2.1 KeV

These uncertainties are reflected directly in the calculated Q-values:

$$\Delta Q(\theta_L) = \Delta E(^6He)$$

4.5 Uncertainty of Scattering Angle Measurements

The second uncertainty in the lab scattering angle is that attached to the actual measurement of the angle. Since the $^1H(^3He,^3He)^1H$ reaction used to measure θ_L is extremely sensitive to angle because of the kinematics of the reaction (1480 KeV/deg at $\theta_L = 11.0°$, E(BEAM) = 68.530 MeV) it is quite insensitive to the beam energy. The angle measurement was therefore assumed good to ± .03°, since this meant determining the outgoing ^3He energy to only ± 45 KeV. The angle uncertainty affects the outgoing ^6He energy two ways; first through the beam energy, since the reaction $^{12}C(^3He,^3He)^{12}C$ and θ_L are used to determine the beam energy, and second, directly through the measured ^6He energy. Fortunately, these two effects tend to cancel one another since the Q-value reflects a difference of incident and outgoing particle energies. This is illustrated in the following example:

Suppose the elastics from $^{12}C(^3He,^3He)^{12}C$ are measured and have energy $E(^3He) = 67.892$ MeV for $\theta_L = 11.0°$ this gives E(BEAM) = 68.530 MeV. For the same outgoing ^3He energy but $\theta_L = 10.0°$, E(BEAM) = 68.420. Now, for the reaction $^{12}C(^3He,^6He)^9C$, these two sets of parameters would yield:

$$E(^6He) = 36.069 \text{ MeV for } E(BEAM) = 68.530,\ \theta_L = 11.0°$$

and

$$E(^6He) = 36.116 \text{ MeV for } E(BEAM) = 68.420,\ \theta_L = 10.0°$$

Therefore, $\Delta E(^6He)$ = 47 KeV/deg for $^{12}C(^3He,^6He)^9C$. The same calculation for the other reactions gives:

$$\Delta E(^6He) = 6 \text{ KeV/deg for } ^{16}O(^3He,^6He)^{13}O$$

$$\Delta E(^6He) = 45 \text{ KeV/deg for } ^{24}Mg(^3He,^6He)^{21}Mg$$

Assuming $\theta_L = \pm .03°$, the uncertainty reflected in the final outgoing ^6He energies and hence the calculated Q-values becomes:

$$\Delta Q(\Delta\theta_L) = \pm 1.4 \text{ KeV for } ^9C$$

$$\Delta Q(\Delta\theta_L) = \pm 0.2 \text{ KeV for } ^{13}O$$

$$\Delta Q(\Delta\theta_L) = \pm 1.4 \text{ KeV for } ^{21}Mg$$

Since such an error in angle determination would be systematic over an entire run, these uncertainties are applied to the average Q-value of each reaction, rather than to each particular measurement.

4.6 ^3He Beam Energy Uncertainties

The systematic uncertainties associated with absolute measurement of the ^3He beam energies are so much a function of the calibration procedure and scattering angle determination, that the values used for ^3He beams are effectively defined by these procedures. Systematic errors in its value has therefore been absorbed into these other uncertainties.

Estimates of the beam energy fluctuations during a run were obtained from the scatter of the ^3He calibration reaction points

over the course of a run. For example, nine individual measurements of the $^{12}C(^{3}He,^{3}He)^{12}C$ elastics over the course of a two day run varied by a maximum of only 8 KeV, with the other calibration reactions showing similar scatter commensurate with their sensitivity to beam energy. This remarkable stability of beam energy was of prime importance to the experiment. The largest such fluctuation for any of the runs was $\Delta E(BEAM) = \pm 10$ KeV.

4.7 Uncertainty in Target Energy Loss

This problem is discussed in the section on target energy loss measurements, and uncertainty values are given there. In the case of the $^{24}Mg(^{3}He,^{6}He)^{21}Mg$ measurement where only one target was used for all measurements, the uncertainty is treated as systematic and applied to the average of the Q-value measurements. For the ^{9}C and ^{13}O measurements several targets were used, and the uncertainties applied to the Q-value measurements for the corresponding targets.

4.8 Stray Magnetic Fields

To guard against spurious effects on incident beam direction due to stray fields of the cyclotron, bending magnets, and particularly the spectrograph whose field was often changed, as well as effects due to the earth's magnetic field, all exposed areas of the beam transport system were wrapped with soft iron for magnetic shielding.

5. EXPERIMENTAL RESULTS

Table 5.1 lists all individual measurements of the Q-values obtained along with the experimental parameters pertinent to each. The column labled "total error" represents all known experimental uncertainties for that point summed in quadrature as though that were the only measurement made. The column labled "partial error" represents the sum (unquadrature) of random errors associated with that particular point.

Table 5.2 lists the resulting average Q-values, their total uncertainties and the resulting values for the mass excesses of ^{9}C, ^{13}O, and ^{21}Mg.

Figure 5.1 displays typical position spectra for the (^{3}He,^{6}He) reactions.

Table 5.1 Experimentally Determined (^{3}He,^{6}He) Q-values

Date	Run Number	Reaction	Q-value (MeV)	Total Error (MeV)	Partial Error (MeV)	^{3}He Beam Energy (MeV)	θ_L (deg)	Target
3/3/70	1-121	$^{12}C(^{3}He,^{6}He)^{9}C$	-31.566	±.020	±.018	68.574±.010	14.82	^{12}C #1
	1-123	$^{16}O(^{3}He,^{6}He)^{13}O$	-31.510	±.020	±.018	68.577±.010	14.82	"Glass"
4/3/70	2-89	$^{12}C(^{3}He,^{6}He)^{9}C$	-31.574	±.011	±.010	68.476±.008	10.96	^{12}C #1
	2-89	$^{12}C(^{3}He,^{6}He)^{9}C$	-31.581	±.011	±.010	68.470±.008	10.96	^{12}C #1
	2-106	$^{12}C(^{3}He,^{6}He)$	-31.597	±.011	±.010	68.470±.008	10.96	^{12}C #1
	2-93	$^{16}O(^{3}He,^{6}He)^{13}O$	-30.506	±.012	±.011	68.476±.008	10.96	SiO, F-80
	2-101	$^{16}O(^{3}He,^{6}He)^{13}O$	-30.524	±.012	±.010	68.470±.008	10.96	SiO, F-80
	2-107	$^{16}O(^{3}He,^{6}He)^{13}O$	-30.504	±.011	±.010	68.470±.008	10.96	SiO, F-80
	2-103	$^{24}Mg(^{3}He,^{6}He)^{21}Mg$	-27.523	±.018	±.013	68.470±.008	10.96	^{24}Mg Foil
	2-108	$^{24}Mg(^{3}He,^{6}He)^{21}Mg$	-27.519	±.017	±.010	68.470±.008	10.96	^{24}Mg Foil
4/12/70	3-15	$^{12}C(^{3}He,^{6}He)^{9}C$	-31.574	±.011	±.010	68.512	11.01	^{12}C #1
	3-27	$^{12}C(^{3}He,^{6}He)^{9}C$	-31.577	±.011	±.009	68.512	11.01	^{12}C #1
	3-17	$^{16}O(^{3}He,^{6}He)^{13}O$	-30.500	±.011	±.010	68.512±.008	11.01	SiO, F-80
	3-28	$^{16}O(^{3}He,^{6}He)^{13}O$	-30.514	±.022	±.012	68.512±.008	11.01	"Glass"

Table 5.1 continued

Date	Run Number	Reaction	Q-value (MeV)	Total Error (MeV)	Partial Error (MeV)	^{3}He Beam Energy (MeV)	θ_L (deg)	Target
4/12/70	3-21	$^{24}Mg(^{3}He,^{6}He)^{21}Mg$	-27.499	±.916	±.009	68.512±.008	11.01	^{24}Mg Foil
	3-29	$^{24}Mg(^{3}He,^{6}He)^{21}Mg$	-27.505	±.017	±.010	68.512±.008	11.01	^{24}Mg Foil
5/30/70	3-88	$^{12}C(^{3}He,^{6}He)^{9}C$	-31.572	±.012	±.011	68.210±.010	10.68	^{12}C "F"
	3-77	$^{12}C(^{3}He,^{6}He)^{9}C$	-31.572	±.013	±.012	68.199±.010	10.68	^{12}C "F"
	3-78	$^{16}O(^{3}He,^{6}He)^{13}O$	-30.478	±.014	±.011	68.199±.010	10.68	SiO+C
	3-89	$^{16}O(^{3}He,^{6}He)^{13}O$	-30.510	±.014	±.011	68.210±.010	10.68	SiO+C
	3-90	$^{16}O(^{3}He,^{6}He)^{13}O$	-30.510	±.014	±.011	68.230±.010	10.67	SiO+C

Table 5.2 Average Q-values and Mass Excesses for the $T_z = -3/2$ Nuclei

Element	Reaction	Q-value (MeV)	Mass Excess (MeV)
^{9}C	$^{12}C(^{3}He,^{6}He)^{9}C$	-31.578±.008	28.911±.009
^{13}O	$^{16}O(^{3}He,^{6}He)^{13}O$	-30.506±.013	23.103±.014
^{21}Mg	$^{24}Mg(^{3}He,^{6}He)^{21}Mg$	-27.512±.018	10.912±.018

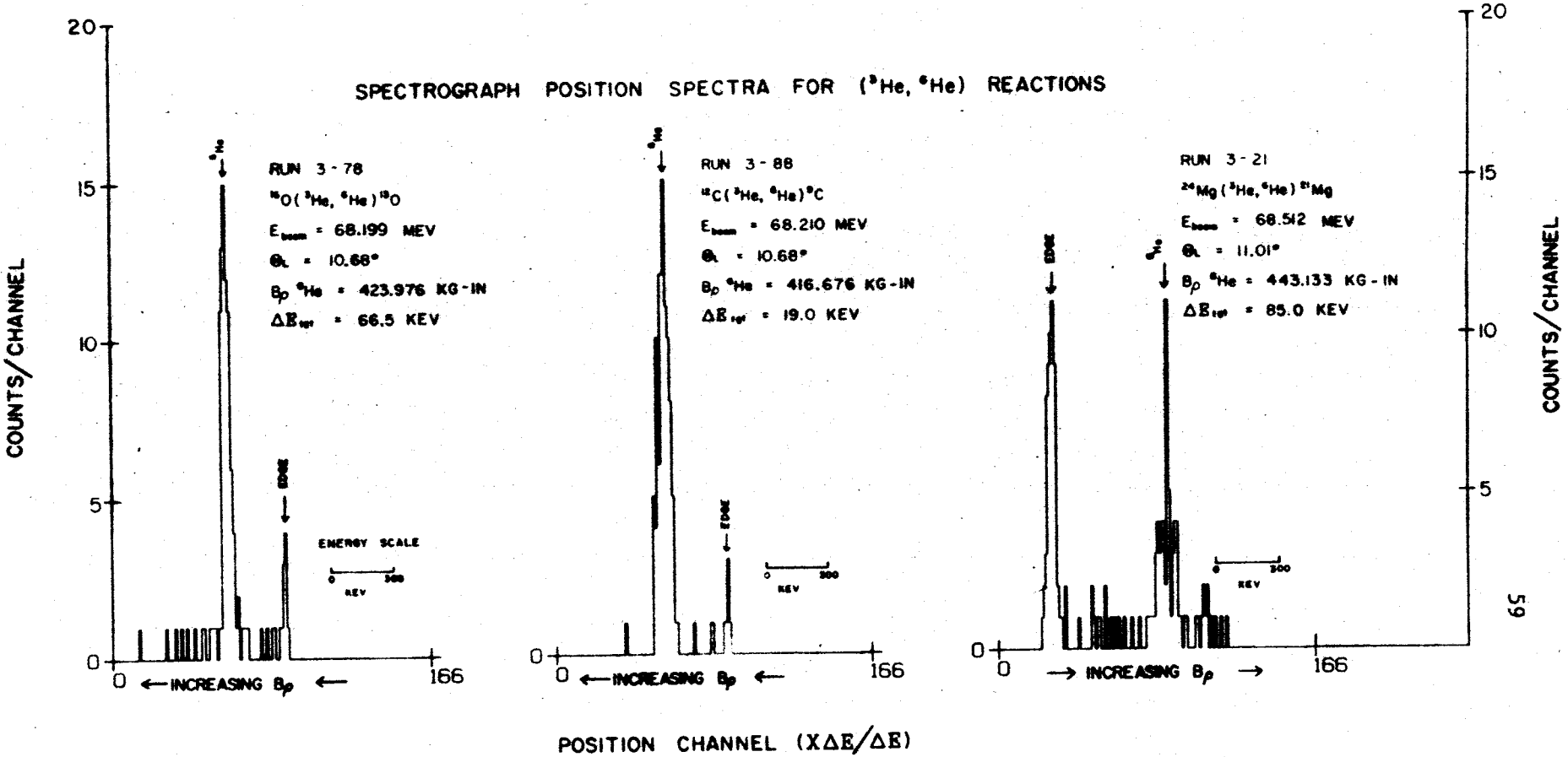

Figure 5.1

(^{3}He, ^{6}He) position spectrum

6. DISCUSSION

Table 6.1 gives the coefficients of IMME for the A = 9, 13, and 21 isobaric quartets. The coefficients $a(\alpha,T)$, $b(\alpha,T)$ and $c(\alpha,T)$ were obtained from a least squares fit of the form

$$M = a + bT_z + cT_z^2$$

to the mass excesses of the quartet members. The $d(\alpha,T)$ coefficient is the coefficient of a T_z^3 term when the same data is fit to the expression

$$M = a + bT_z + cT_z^2 + dT_z^3$$

For both cases the mass excess values for the $T_z = -3/2$ members are taken from Table 1 of (Ga 69). The term ^{2} represents the quality of the fit, and the expression used was

$$^2 = \sum_1 \left[\frac{M(calc) - M(exp)}{\sigma M(exp)}\right]^{1/2}$$

Deviations of the experimentally determined masses and predictions of the IMME with a, b, and c coefficients of Table 6.1 are displayed graphically in Figure 6.1. Only the A = 9 quartet shows deviations greater than the experimental uncertainty of the points.

The addition of higher order terms such as T_z^3 and T_z^4 to the IMME are predicted when the Coulomb potential is expanded as a second order perturbation. Such a second order treatment then involves mixing of states of T(perturb) = T±1 through the off diagonal matrix elements of the expansion. This has been done in detail in a recent article by

Janecke (Ja 69), where the IMME is expanded to a quartic in T_z. The conclusion reached here is that terms in T_z^3 and T_z^4 will be small, not so much because the perturbation is small, but because the major effects of such perturbations are absorbed mostly in the T_z, and T_z^2 terms.

The size of the d coefficient (of dT_z^3) has been estimated to be $\approx Z\alpha c$ (Ga 69) where Z is the average charge of the multiplet, α is the fine structure constant, and c the coefficient of T_z^2. For the A = 9 quartet this would be ≈9 KeV and the data indicates a d term of this magnitude. For A = 13 and 21 such a term is not evident.

The determination of such a cubic term from isobaric quartets must be done with caution. Since the cubic will fit a quartet exactly, the d term and its uncertainty may be expressed in terms of the masses:

$$d = \frac{M(3/2) - M(-3/2) - 3\{M(1/2) - M(-1/2)\}}{6}$$

$$\Delta d = \frac{\Delta M(3/2) + \Delta M(-3/2) + 3\{\Delta M(1/2) + \Delta M(-1/2)\}}{6}$$

where M is the mass of the multiplet member whose T_z value is in paranthesis. From these expressions, it is apparent that the generally small experimental uncertainties of the $T_z = \pm 1/2$ members (≈ ±5 KeV) may contribute as much or more to the uncertainty in d as the larger uncertainties of the $T_z = \pm 3/2$ members. For this reason, careful determination of all member masses is required.

Another attempt to make some estimate of the size of the d term

is presented in (He 69), where the Schroedinger equation is solved directly for a nuclear model. The model consists of three nucleons outside an inert core, with each of these extra nucleons in a Woods-Saxon nuclear potential, a Lane symetry potential, and the Coulomb potential of a uniformly charged sphere with radius equal to that of the Woods-Saxon well. The coefficients for the T_z and T_z^2 terms agree with experimental values, generally to within 10 - 20%. The predicted d term, however, is on the order of several hundred eV rather than the $\approx$9 KeV ($Z\alpha c$) estimate. Such values are not inconsistent with those of A = 13 and 21 of Table 6.1.

Because many charge dependent effects may be absorbed into the T_z and T_z^2 terms, the quadratic form of the IMME fits data well over a wide range of mass values (Table 2 in Ga 69, for example). This quality provides confidence that the quadratic IMME may be used to extrapolate to unknown masses with good accuracy. This has been done, for example, to determine the mass of ^{25}Si (Wi 70).

Several attempts to extract specific information from a study of the IMME coefficients (Ja 66 and Wil 64) but were limited to some extent by the quantity and quality of data available on $T \geq 1$ multiplets.

The uniformly charged sphere model serves as an example of how information may be extracted from the coefficients. For a Coulomb energy of

$$V_C = \frac{3}{5} \frac{Z(Z-1)\, e^2}{R_C}$$

the term $Z(Z - 1)$ may be expanded in terms of T_z and T_z^2 to yield the

IMME coefficients (Ga 69):

$$b = -\frac{3}{5}\frac{(A-1)e^2}{R_o A^{1/3}} + (M_n - M_p)$$

$$c = \frac{3}{5}\frac{e^2}{R_o A^{1/3}}$$

A is the mass number of the multiplet and $(M_n - M_p)$ the neutron-proton mass difference. The Coulomb radii R_o may be obtained for known b and c coefficients, and these radii are given in Table 6.2. The validity of such a model will be reflected in the values of the radii, and in their consistency. In addition, the radius values should be the same whether extracted from the b or c coefficient.

The radii from Table 6.2 are reasonable and compare with those of various models (No 69, for example). This would indicate that such a Coulomb potential is a major contributor to T_z and T_z^2 dependence. The fact that the b and c coefficients yield different results, however, indicates that other effects are also present. An attempt to reduce this effect by deforming the sphere yields negative results since such a reduction in the Coulomb energy could not account for the fact that for A = 37 the ratio $\frac{R(c)}{R(b)} > 1$ while it is less than one for the other multiplets. Estimates of the deformation effect also indicate that changes in the $\frac{R(c)}{R(b)}$ ratio would be small. The failure of this simple model to reproduce these effects indicates that charge dependent interactions in addition to the Coulomb interaction are contributing to the T_z and T_z^2 terms.

A detailed study of the coefficients to obtain specific information on the Coulomb systematics requires good experimental measurements of high T multiplet members. In addition, the determination of excited levels in the $T_z = -3/2$ members would be valuable for comparison with structure of the other multiplet members. The experimental procedures developed in this work will, in addition to making absolute Q-value measurements at high bombarding energy possible with high precision, allow study of neutron deficient nuclei and thus aid in the study of the Coulomb systematics of high T multiplets.

Table 6.1 Empirically determined coefficients for the mass equation $M = a + bT_z + cT_z^2$. The last column indicates the coefficient of a T_z^3 term assuming the equation to have the form $M = a + bT_z + cT_z^2 + dT_z^3$.

Mass	a(a,T) MeV	b(a,T) MeV	c(a,T) MeV	χ^2	d(a,T) KeV
9	26.343±.004	-1.3185±.003	0.266±.003	4.0	0.0083±.0039
13	19.257±.0027	-2.1802±.0035	0.256±.003	.002	-0.0002±.0035
21	4.8987±.0046	-3.6573±.005	0.240±.0048	1.28	0.0057±.0051

Table 6.2 Coulomb Radii from the IMME Coefficients

Mass A	b(α,T) (MeV)	R_o(b) (Fermi)	c(,T) (MeV)	R_o(c) Fermi
9	-1.319[a]	1.581	.266[a]	1.562
13	-2.180[a]	1.489	.256[a]	1.436
17	-2.878[b]	1.469	.238[b]	1.412
21	-3.657[a]	1.411	.240[a]	1.305
23	-3.960[c]	1.409	.223[c]	1.362
25	-4.387[b]	1.372	.216[b]	1.368
37	-6.181[b]	1.340	.174[b]	1.490

[a] Present work

[b] See (Me 70)

[c] See (Ga 69)

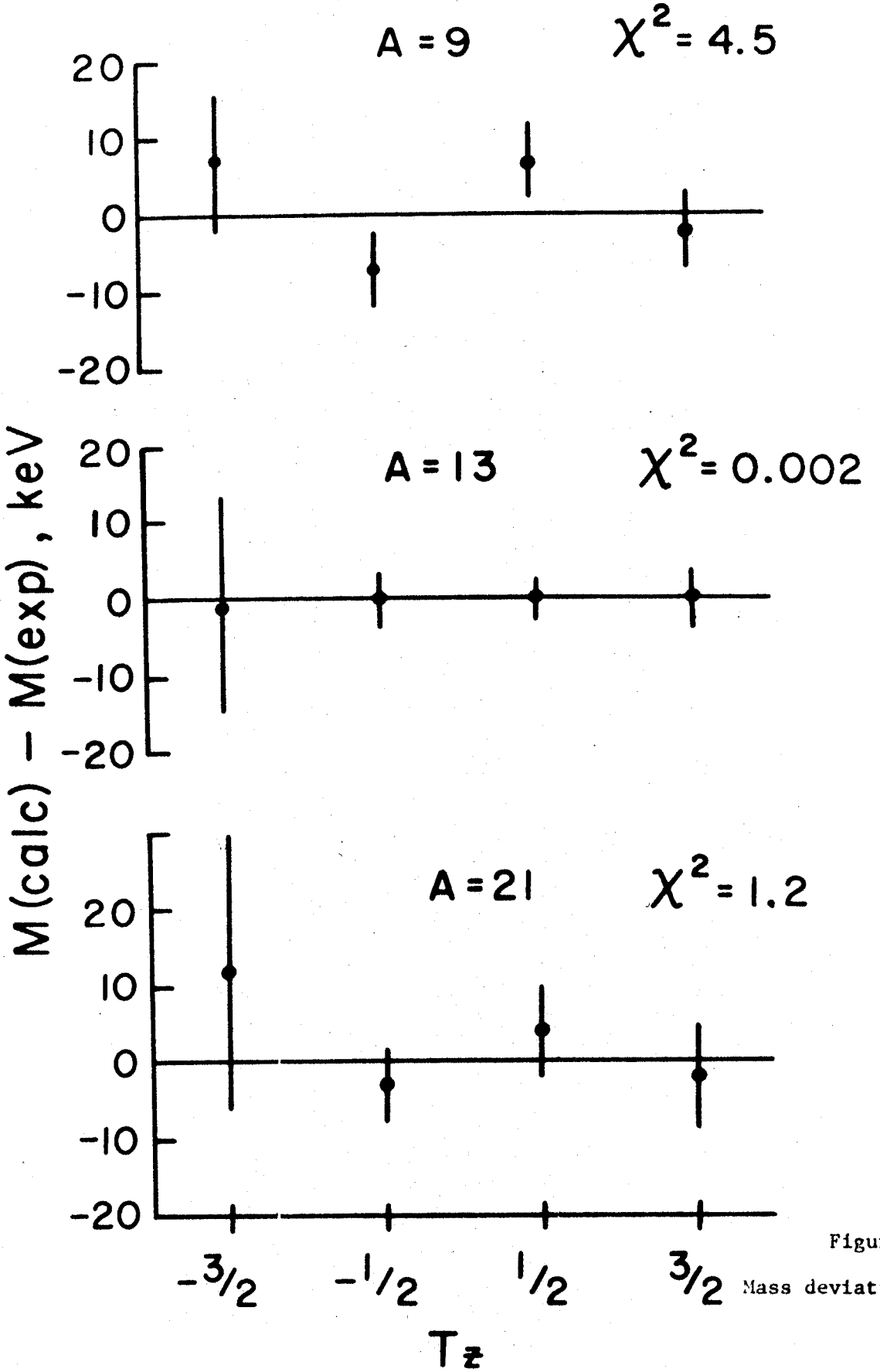

Figure 6.1

Mass deviations from IMM

APPENDIX

APPENDIX A1

Derivation of the Isobaric Multiplet Mass Equation (IMME)

The IMME:

$$M(\alpha,T,T_z) = a(\alpha,T) + b(\alpha,T)T_z + c(\alpha,T)T_z^2$$

may be derived from first order perturbation theory with the following assumptions: the Coulomb potential is two-body, and is a perturbation on the nuclear potential, and all members of an isobaric multiplet are identical in their charge independent characteristics. The charge independent characteristics are denoted by α in the equation. Then for

$$Vc = \sum_{i>j} \frac{e^2}{rij} (1/2 - t_{zi})(1/2 - t_{zj})$$

where t_z is the isospin value +1/2 for neutrons and -1/2 for neutrons, and r_{ij} is their relative separation, the expression for V_c becomes:

$$V_c = \sum_{i>j} \frac{e^2}{r_{ij}} (1/4 - 1/2(t_{zi} + t_{zj}) + t_{zi}t_{zj})$$

and judicious addition of a term $\frac{t_{zi}\cdot t_{zj}}{3}$ yields

$$V_c = \left[\sum_{i>j} \frac{e^2}{r_{ij}} (1/2) + \frac{(t_{zi}\cdot t_{zj})}{3}\right] - \left[\sum_{i>j} \frac{e^2}{2r_{ij}} (t_{zi}+t_{zj})\right]$$

$$+ \left[\sum_{i>j} \frac{e^2}{r_{ij}} (t_{zi}t_{zj} - \frac{t_{zi}\cdot t_{zj}}{3})\right]$$

The Coulomb potential has thus been separated into tensor operators $V_c(0)$, $V_c(1)$, and $V_c(2)$ of rank 0, 1, 2, and the perturbing Coulomb term $\langle \alpha TT_z | V_c | < TT_z \rangle$ may be reduced with respect to isospin:

$$\langle \alpha,T,T_z | V_c | \alpha,TT_z \rangle = \langle \alpha,TT_z | V(0) | \alpha TT_z \rangle$$

$$\langle \alpha,TT_z | V(1) | \alpha TT_z \rangle$$

$$\langle \alpha,TT_z | V(2) | \alpha TT_z \rangle$$

using the Wigner-Ekhart theorem this becomes:

$$\langle \alpha,TT_z | V(0) | \alpha TT_z \rangle = \langle T0T_z0 | TT_z \rangle \langle \alpha,T \| V(0) \| \alpha,T \rangle$$

$$\langle \alpha,TT_z | V(1) | \alpha TT_z \rangle = \langle T1T_zT_z | TT_z \rangle \langle \alpha,T \| V(1) \| \alpha,T \rangle$$

$$\langle \alpha,TT_z | V(2) | \alpha TT_z \rangle = \langle T2T_zT_z | TT_z \rangle \langle \alpha,T \| V(2) \| \alpha,T \rangle$$

where the double bracket represents matrix elements reduced w.r.t. isospin. The Clebsch-Gordon coefficients are:

$$\langle T0T_z0 | TT_z \rangle = 1$$

$$\langle T1T_zT_z | TT_z \rangle = \frac{T_z}{[T(T+1)]^{1/2}}$$

$$\langle T2T_zT_z | TT_z \rangle = \frac{3T_z^2 - T(T+1)}{[(2T-1)T(T+1)(2T+3)]^{1/2}}$$

Since T is a constant for a given multiplet the Coulomb perturbation then becomes

$$\langle \alpha,TT_z | V_c | \alpha,TT_z \rangle = a(\alpha,T) + b(\alpha,T)T_z + c(\alpha,T)T_z^2$$

The mass difference between the proton and neutron which must be taken into account between the members of an isobaric multiplet may be written:

$$V(\Delta m) = \frac{(M_n+M_p)}{2}A + (M_n-M_p)T_z$$

and may therefore be absorbed into the IMME since it is linear in T_z.

LIST OF REFERENCES

Aj 66 T. Lauritsen and F. Ajzenberg-SeLove, Nucl. Phys. 78 (1966) No. 1 pp 24

An 62 J. D. Anderson, C. Wong, and J. W. McLure, Phys. Rev. 126, 2170 (1962)

Ba 69 D. Bayer, Bull. Am. Phys. Soc., (1969)

Be 57 Yardley Beers, Introduction to the Theory of Error, Addison-Wesley, Reading, Mass. (1957)

Ce 68 J. Cerny, Ann. Rev. of Nucl. Sci., 18 (1968) pp 27

Ch 67 C. Chasman, K. W. Jones, R. A. Ristinen, D. E. Alburger, Phys. Rev. 159 (1967) pp 830

Da 69 Guide to the Selection and Use of Position Sensitive Detectors, Nuclear Diodes (1969) ed. by W. W. Daehnick

En 58 H. A. Enge, Review of Scientific Instruments, 29 (1958) pp 885

Ga 69 G. T. Garvey, Nuclear Isospin, Proceedings of the Conference on Nuclear Isospin at Asilomar, ed. by J. D. Anderson, S. D. Bloom, J. Cerny, and W. W. True, Academic Press, New York, 703 (1969)

He 69 E. M. Henley and C. E. Lacy, Phy. Rev. 184 (1969) pp 1228

Ja 69 Joachim Janecke, Nuclear Physics A128 (1969) 632

Jo 70 R. K. Jolly, G. F. Trentelman and E. Kashy to be published in Nuclear Instruments and Methods

Ka 70 E. Kashy, R. K. Jolly, and G. F. Trentelman, to be published

Ma 66 C. Maples, G. W. Goth and J. Cerny, Nuclear Reaction Q-values Lawrence Radiation Laboratory, Berkeley, California, UCRL-16964 (1966)

Ma 67 G. H. Mackenzie, E. Kashy, M. M. Gordon, and H. G. Blosser, The Beam Transport System of the Michigan State University Cyclotron. IEEE Transactions on Nuclear Science Vol. NS-14, No. 3, 450 (1967)

Mar 67 J. B. Marion, University of Maryland Technical Report #ORO-2098-58 (1967)

No 69 J. A. Nolen and J. P. Schiffer, Coulomb Energies, University of Maryland Technical Report No. 70-035 (1970)

Sn 67 J. L. Snelgrove and E. Kashy, Nucl. Inst. and Meth. 52 (1967) pp 153

Sp 67 J. E. Spencer and H. A. Enge, Nucl. Inst. and Meth. 49 (1967) pp 181

Te 69 B. Teitelman and G. M. Temmer, Phys. Rev. 177 1656 (1969)

Tr 70 G. F. Trentelman and E. Kashy, to be published in Nuclear Instruments and Methods

Wa 65 E. K. Warburton, J. W. Olness, D. E. Alburger, Phys. Rev. 140 B1202 (1965)

Wia 66 C. F. Williamson, J. P. Boujot, J. Picard, Tables of Range and Stopping Powers of Chemical Elements for Charged Particles of Energy 0.05 to 500 MeV, Centre D'Etudes Nucléaires De Saclay, CEA-R3042 (1966)

Wi 57 E. P. Wigner, Isospin-A Quantum Number for Nuclei Proceedings of the Robert A. Welch Foundation Conferences on Chemical Research, I. The Structure of the Nucleus (1957) Houston, Texas

Wi 64 D. H. Wilkinson, Phys. Rev. Letters, 13, No. 19 (1964) pp 571, Physics Letters, Vol 12 No. 4, (1964) pp 348

Wi 64 D. H. Wilkinson, Phys. Rev. Letters, 13 (1964) pp 571

Wi 69 D. H. Wilkinson and D. E. Alburger, Phys. Rev. Letters, 24 (1969) pp 1134

Me 70 R. Mendelson, G. J. Wozniak, A. D. Bacher, J. M. Loiseaux, and J. Cerny, submitted to Phys. Rev. Letters (1970)

Ja 66 Joachim Janecke, Phys. Rev. 147 (1966) pp 735